



Originally published as:

Bauer, K., Moeck, I., Norden, B., Schulze, A., Weber, M., Wirth, H. (2010): Tomographic P-wave velocity and vertical velocity gradient structure across the geothermal site Gross Schoenebeck (NE German Basin): Relationship to lithology, salt tectonics, and thermal structure. - Journal of Geophysical Research, VOL. 115, B08312

DOI: 10.1029/2009JB006895

Tomographic *P* wave velocity and vertical velocity gradient structure across the geothermal site Groß Schönebeck (NE German Basin): Relationship to lithology, salt tectonics, and thermal regime

K. Bauer,¹ I. Moeck,¹ B. Norden,¹ A. Schulze,¹ M. Weber,^{1,2} and H. Wirth³

Received 21 August 2009; revised 10 March 2010; accepted 26 March 2010; published 25 August 2010.

[1] Seismic wide-angle data were collected along a 40-km-long profile centered at the geothermal research well GrSk 3/90 in the Northeast German Basin. Tomographic inversion of travel time data provided a velocity and a vertical velocity gradient model, indicative of Cenozoic to Pre-Permian sediments. Wide-angle reflections are modeled and interpreted as top Zechstein and top Pre-Permian. Changes in velocity gradients are interpreted as the transition from mechanical to chemical compaction at 2–3 km depth, and localized salt structures are imaged, suggesting a previously unknown salt pillow in the southern part of the seismic profile. The Zechstein salt shows decreased velocities in the adjacent salt pillows compared to the salt lows, which is confirmed by sonic log data. This decrease in velocity could be explained by the mobilization of less dense salt, which moved and formed the salt pillows, whereas the denser salt remained in place at the salt lows. We interpret a narrow subvertical low-velocity zone under the salt pillow at GrSk 3/90 as a fault in the deep Permian to Pre-Permian. This WNW-ESE trending fault influenced the location of the salt tectonics and led to the formation of a fault-bounded graben in the Rotliegend sandstones with optimal mechanical conditions for geothermal production. Thermal modeling showed that salt pillows are related to chimney effects, a decrease in temperature, and increasing velocity. The assumed variations in salt lithology, density, and strain must thus be even higher to compensate for the temperature effect.

Citation: Bauer, K., I. Moeck, B. Norden, A. Schulze, M. Weber, and H. Wirth (2010), Tomographic *P* wave velocity and vertical velocity gradient structure across the geothermal site Groß Schönebeck (NE German Basin): Relationship to lithology, salt tectonics, and thermal regime, *J. Geophys. Res.*, 115, B08312, doi:10.1029/2009JB006895.

1. Introduction

[2] Geophysical methods provide basic information required to determine optimal sites for the utilization of geothermal energy. Major topics to be addressed in geothermal exploration include (1) the general geological structure and lithostratigraphy, (2) information on the temperature field, (3) the location of major faults both around the reservoir and at deeper levels, and (4) the distribution of fluids. Seismic methods are highly developed in hydrocarbon exploration and can be adopted to contribute to these items. Refraction seismic profiling and tomographic inversion techniques are well suited to determine the velocity structure. Seismic velocities are sensitive to the lithological structure, major

faults with reduced velocity, and fluid-bearing horizons. The combination of velocity tomography with preexisting or new seismic reflection data can significantly improve the knowledge of the structure and composition. Deeper levels underneath the geothermal system can be resolved by seismic tomography, whereas seismic reflection data exhibit less certain information, e.g., on the existence of deep reaching faults. Faults are important for the geothermal system because they can channel rising deeper (hotter) fluids which may represent a major heat source [Baechler *et al.*, 2003]. Furthermore, the results from tomography can be combined with thermal modeling using the relationship between seismic velocity and temperature [e.g., Schoen, 1996]. The idea of such a combined analysis would be to test whether the velocity structure reflects variations in the temperature field as an important outcome for the geothermal exploration.

[3] This paper presents results from a seismic refraction tomography experiment across the geothermal site near Groß Schönebeck, located ~30 km north of Berlin in the Northeast German Basin (NEGB) (Figure 1). This study is part of the “Integrated Geophysical Exploration Technologies for deep fractured geothermal reservoirs” (I-GET) project,

¹Deutsches GeoForschungsZentrum GFZ, Potsdam, Germany.

²Also with Department of Geosciences, University of Potsdam, Potsdam, Germany.

³Bundesanstalt für Geowissenschaften und Rohstoffe (BGR), Berlin/Hannover, Germany.

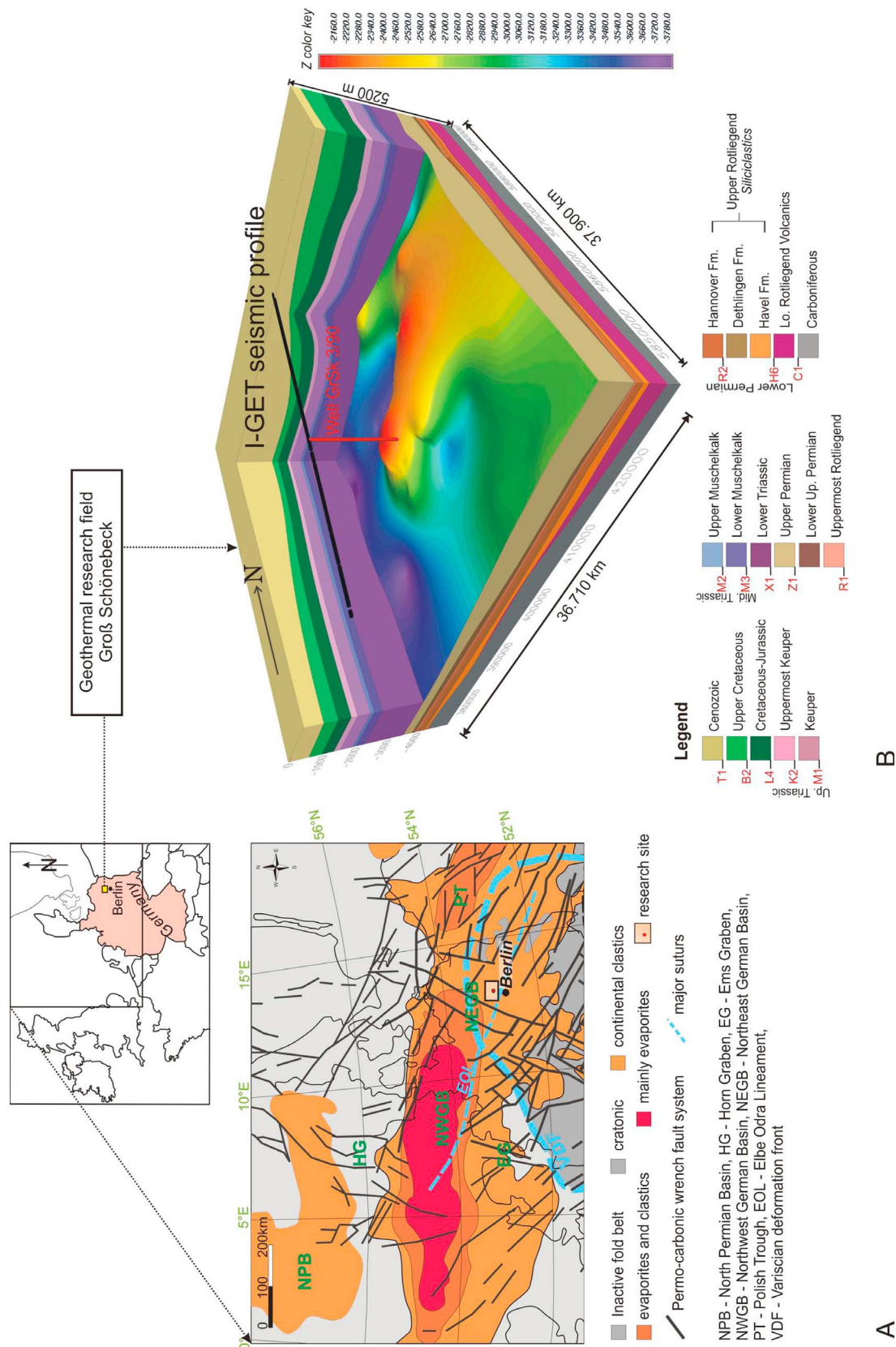


Figure 1. (a) Structural lithofacies map of the Lower Permian (Rotliegend) in the Central European Basin System (synthesis of *Gast and Gundlach* [2006], *Ziegler and Dezés* [2006], *Ziegler* [1990], and *Scheck et al.* [2002]). (b) 3-D structural model of the Groß Schönebeck area developed from existing seismic reflection and well data [*Moeck et al.*, 2009]. The contours show the topography of the evaporite layers. Inset shows the location of the study area.

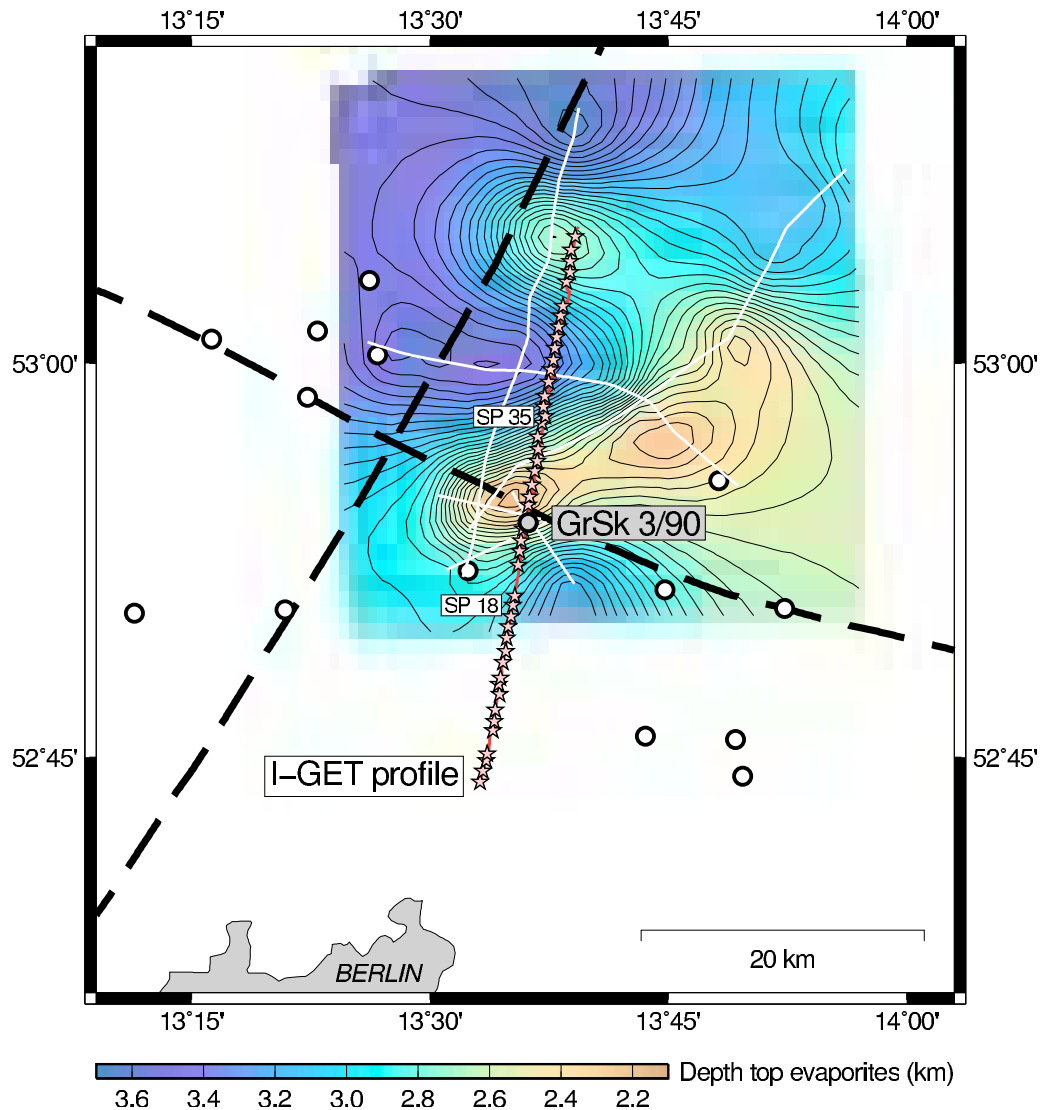


Figure 2. Location map of the “Integrated Geophysical Exploration Technologies for deep fractured geothermal reservoirs” (I-GET) project seismic experiment. The red line marks the receiver spread, and the stars represent shot locations along the 40-km-long profile, centered at the geothermal research well GrSk 3/90. The contour map shows the depth distribution for the top of the evaporite sequence on the basis of preexisting industry seismic reflection data (white lines) and bore hole information [Moeck *et al.*, 2009]. Deep fault zones (after Katzung [1990]) are shown as dashed lines.

a European Union-funded initiative to develop integrated exploration methods for fractured and/or porous fluid-bearing geothermal systems. Exploration techniques are tested in I-GET at four typical sites in volcanic, metamorphic, and sedimentary environments in Europe. Groß Schönebeck was selected as a prototype for a low- to medium-enthalpy geothermal system to be established under conditions commonly found in sedimentary basins. The target horizons to be used consist of Lower Permian (Rotliegend) sandstones and volcanic rocks at depths between 3.9 and 4.4 km. These rocks were deposited during the initial stages of the developing Southern Permian Basin. At this depth range, typically temperatures of $\sim 150^{\circ}\text{C}$ are encountered [e.g., Huenges *et al.*, 2007], sufficient for electrical power generation. The thick

evaporitic deposits of the Upper Permian are a dominant feature within the sedimentary succession above the reservoir layers in the NEGB. An important, still open question with relevance for geothermal exploration is how the salt architecture and its tectonic history influences the geomechanical and thermal conditions at the reservoir level below it.

[4] The new study was embedded within the preexisting geological and geophysical knowledge of the study area. This background information is described in the next section. The new data from the I-GET experiment are then presented, and the derivation of the seismic velocity model is demonstrated for the different stages of the inversion process. In the discussion, the results from tomography are integrated with seismic reflection data, borehole informa-

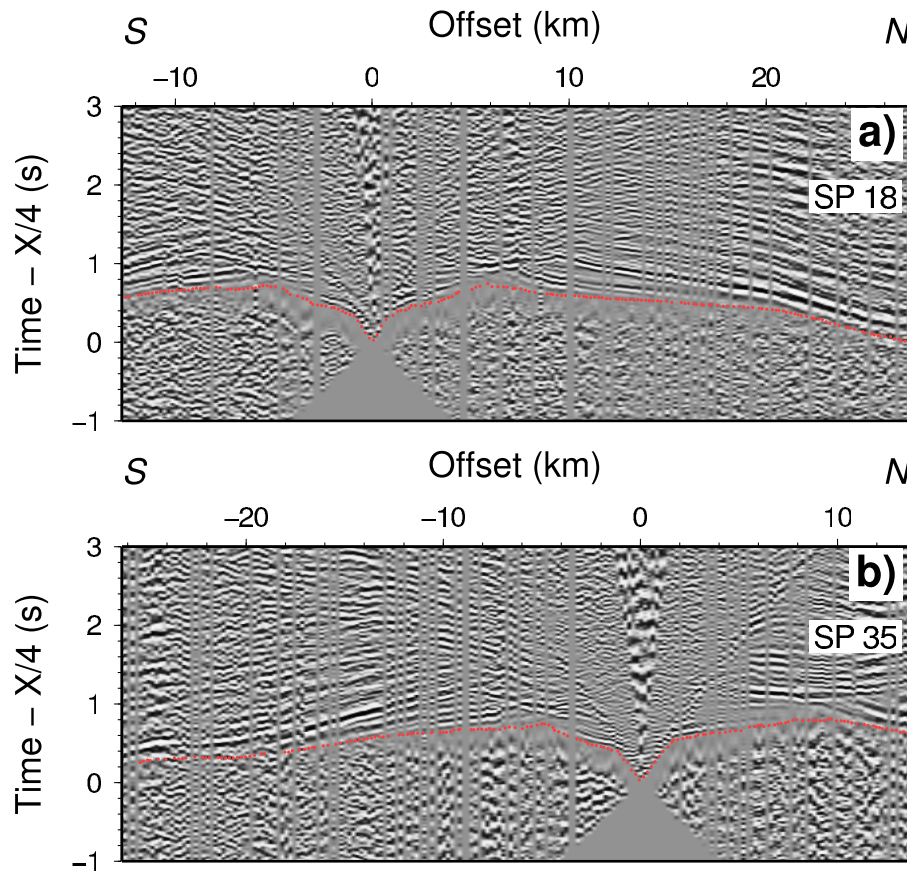


Figure 3. Shot gathers for two source locations (a) shot point SP 18, and (b) shot point SP 35. Locations are shown in Figure 2. The data are band-pass-filtered from 4 to 15 Hz and plotted with 4-km/s reduction velocity. First arrival travel times (red dots) were determined by repeated picking and subsequent averaging.

tion, geological interpretation, and thermal modeling to explain the regime at the geothermal target region.

2. Geological Setting and Preexisting Geophysical Data

[5] The NEGB is a sub-basin of the complex Central European Basin System (CEBS) that extends from the Norwegian-Danish Basin over the North German Basin westward to the Polish Basin [e.g., *Scheck-Wenderoth and Lamarche*, 2005]. The North German Basin is subdivided in a northwestern and northeastern branch on the basis of different structural styles which have been investigated on a regional rather than a reservoir scale [*Baldschuhn et al.*, 2001; *Kaiser et al.*, 2005; *Marotta et al.*, 2000; *Maystrenko et al.*, 2005; *Hansen et al.*, 2007]. The CEBS is a complex sedimentary basin in which >10 km of sediments accumulated during >260 million years under varying stress and sedimentary regimes [*Littke et al.*, 2005]. It provides therefore a complex geological pattern, and the NEGB, as part of the CEBS, represents an example for long-living multiphase basins. Despite several existing 3-D structural and kinematic models for the southern and central parts of the NEGB [*Bayer et al.*, 1997; *Hansen et al.*, 2007; *Scheck et al.*, 1999; *Scheck et al.*, 2003a; *Scheck et al.*, 2003b;] and also the adjacent Polish Basin [*Lamarche et al.*, 2003; *Lamarche and Scheck-*

Wenderoth, 2005], geophysical-geological models on a reservoir scale suitable for geothermal exploration are still not available. An early structural model on reservoir scale was derived by *Moeck et al.* [2009], using reprocessed 2-D seismic reflection data and well data from former gas exploration in the Groß Schönebeck area (see preexisting profiles and well locations in Figure 2). This geological model, covering an area of 40 × 40 km, describes the lithology and the overall structural pattern incorporating major fault systems in the Groß Schönebeck area from 5 km depth to surface.

[6] With the cessation of the Variscian consolidation of central Europe, the basin initiation started in the early Permian with a short phase of enormous volcanism [*Benek et al.*, 1996], followed by a rapid phase of initial thermal subsidence that continued until the end of Middle Triassic [*Kossow et al.*, 2000; *Littke et al.*, 2005; *van Wees et al.*, 2000]. The oldest deposits in the NEGB consist consequently of Carboniferous-Permian volcanic rock (Andesite) overlain by aeolian, fluvial, and lacustrine sediments of Lower Permian (Rotliegend) age. This Lower Permian succession represents a geothermal reservoir because a sequence of medium-grained highly porous sandstone hosts a hydrothermal aquifer system [*Huenges et al.*, 2007; *Moeck et al.*, 2009]. These siliciclastic sediments are overlain by Upper Permian (Zechstein) evaporites which locally increase in thickness up to 1.2 km at the Groß Schönebeck site, or even

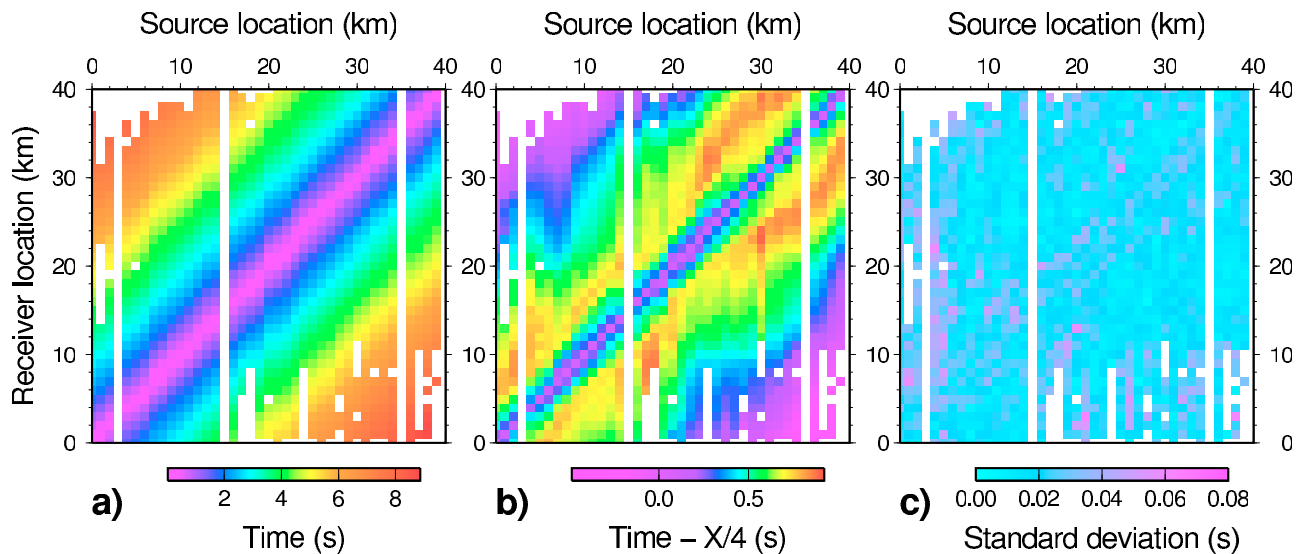


Figure 4. First arrival travel times (a) unreduced and (b) reduced with a 4-km/s reduction velocity as a function of source and receiver location. (c) Standard deviations of first arrival travel times determined from repeated picking. A 2-D grid was used with a source distance increment of 1 km (nominal shot spacing 800 m) and a receiver distance increment of 1 km (receiver spacing was 200 m).

more in regions of diapirism [Moeck *et al.*, 2009; Scheck and Bayer, 1999]. Above and below the salt, the fault systems differ and are decoupled by the Zechstein evaporites. The overburden structure is strongly influenced by salt tectonics which started in the Late Triassic and culminated in the Upper Cretaceous to Middle Tertiary [Jaritz, 1987]. In particular, the dominating Mesozoic structure at the Groß Schönebeck site is an antiform above a N 70°E trending salt ridge at which the geothermal research well GrSk 3/90 is located. The salt moved upward to a depth of 2.1 km (Figure 1b). In the northwest of the model area, ~10 km north of the well GrSk 3/90, the reduced thickness of the salt implies salt mobilization resulting in a depression in the suprasalt successions.

[7] The Triassic succession consists of the terrestrial Lower Triassic clastic red-bed sequence (Buntsandstein), overlain by marine carbonates of Middle Triassic age (Muschelkalk). Renewed terrestrial sedimentation effectuated the deposition of clay stones, siltstones, and sandstones during the Upper Triassic (Keuper), followed by a sequence of marl, clay stone, and sandstone of Lower Jurassic age (Liassic). A hiatus between Middle Jurassic and late Lower Cretaceous (Figure 1) was caused by a basinwide uplift and subsequent erosion [Kossow *et al.*, 2000] probably reinforced by local salt tectonics. Late Lower Cretaceous clastic sediments are followed by Upper Cretaceous marine marls and carbonates, overlain by Cenozoic deposits, whose distribution and thickness are partly influenced by salt tectonics. Presumably, the sediments in the rim synclines between salt structures exhibit different porosity and cementation than the sediments at the top of salt highs.

[8] The subsalt fault system is dominated by northwest striking major faults and north to northeast trending minor faults. The throw along the faults indicates downward movement of the hanging walls by a few meters. This fault system may have been part of the regional wrench fault system, which was active in the postorogenic period of the

variscan orogeny [Ziegler and Dezès, 2006]. There are no indications of reverse faulting in the modeled area. The suprasalt fault system is irregular but exhibits a larger fault density above salt highs [Moeck *et al.*, 2009], indicating high strain rates during salt movement accommodated by a larger number of dilatational faults. Data for the suprasalt fault system is sparse, suggesting a more heterogeneous orientation of faults [Roth and Fleckenstein, 2001].

3. Seismic Experiment and Field Data

[9] A 40-km-long seismic profile centered on the location of the GrSk 3/90 borehole was conducted to study the seismic velocity structure around the geothermal reservoir at the regional scale (Figure 2). The experimental setup was designed to allow for the application of 2-D refraction tomography methods and for the analysis of wide-angle reflections typically observed with such layouts. A length of 40 km was required to guarantee a sufficient illumination of the reservoir layers at 4 km depth. The orientation of the profile was chosen approximately parallel to the major horizontal component of the current regional stress field. The transect crosses at least two salt highs and the corresponding intermediate salt lows (see top of Zechstein salt in Figure 2, taken from the 3-D geological model in Figure 1).

[10] The survey utilized 45 explosive shots that were distributed along the profile at an average spacing of 800 m. The shots consisted of 20–30 kg explosives in 15-m-deep bore holes. A constant receiver spread deployed along the entire profile was used to record the shots. One hundred ninety channels with 4.5-Hz, three-component sensors were spaced at 200 m along the seismic profile. The data were sampled at 5 ms and are of good quality. Examples from two shot locations are shown in Figure 3. The data are band pass filtered (Ormsby minimum phase filter 2–4 to 15–25 Hz) and are plotted with 4 km/s reduction velocity. The

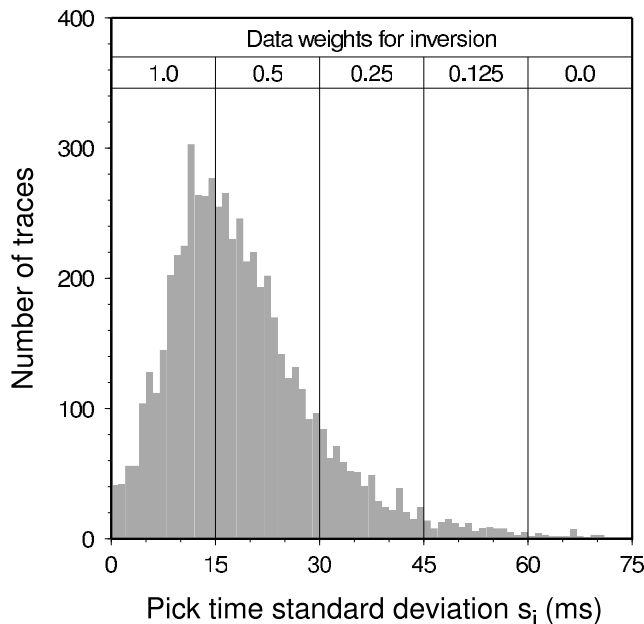


Figure 5. Histogram of the travel time standard deviations derived from repeated picking of first arrivals. The standard deviations are used to define the quality of the individual picks. Five quality categories are defined (standard deviations of 0–15, 15–30, 30–45, 45–60, >60 ms) and corresponding data weights assigned (1.0, 0.5, 0.25, 0.125, 0) for the travel time inversion.

first arrivals used to develop the tomographic velocity model can be followed to maximum distances of 25–35 km and have dominant frequencies of 8–12 Hz.

4. Seismic Velocity Modeling and Inversion

[11] The seismic data were used to derive a 2-D velocity model. The general approach for the development of the velocity model was to systematically increase the number of model parameters during the different stages of the modeling process. The working flow included (1) determination of the travel times and uncertainties of the direct *P* wave arrivals, (2) forward modeling and inversion to derive the optimal 1-D model, (3) a subsequent 2-D tomographic inversion, and (4) resolution analysis to evaluate the uncertainty of the final 2-D model.

4.1. Travel Time Data

[12] Preparation of the data for travel time picking included geometry installation, trace editing, band pass filtering, and linear move-out correction (see examples in Figure 3). The determination of arrival times was carried out by manual picking of the first extremum of the waveforms and subtraction of a quarter period of the average dominant frequency (10 Hz). Manual travel time picking was repeated several times to obtain a number of arrival time values for each trace. The approach of repeated travel time determination has two advantages: (1) mispicks are not used as single data values in the inversion but are statistically averaged, and (2) individual data errors can be derived directly from the picking process without statistical assumptions and can be

used for data weighting in the tomographic inversion. Average travel \bar{t}_i times were determined for each trace *i* from a number of picks N_i with travel times t_{ik} :

$$\bar{t}_i = \frac{1}{N_i} \sum_{k=1}^{N_i} t_{ik}, \quad (1)$$

where N_i typically varied between 5 and 15. To account for the relatively small number of values per trace, the sample standard deviation s_i was used to provide an unbiased parameter estimation for the pick uncertainty:

$$s_i = \sqrt{\frac{1}{(N_i - 1)} \sum_{k=1}^{N_i} (t_{ik} - \bar{t}_i)^2}. \quad (2)$$

[13] An overview with all averaged travel time values as a function of source and receiver locations is given in Figure 4 (unreduced and with 4 km/s reduction velocity, respectively). In this kind of presentation, zero offset corresponds to the diagonal trace (same source and receiver location), and any parallel translation of this trace corresponds to distinct source-receiver offsets and a certain depth of penetration. Particularly, the plot with reduction velocity of 4 km/s (Figure 4b) already clearly reflects the variations of the travel time function along the profile for specific offsets and related depth of penetration. This is an initial indication for the lateral variations of the 2-D velocity structure along the seismic profile.

[14] The standard deviations calculated from repeated determinations of the first arrival travel times are shown as a function of source and receiver locations (Figure 4c), as well as their distribution in a histogram (Figure 5). The errors are caused by the variations in the data evaluation during the manual picking. Ninety percent of the travel times were picked with standard errors <30 ms. This value corresponds to approximately a quarter period of the 8–12 Hz signals, which is in agreement with other studies [e.g., Zelt *et al.*, 2006]. The error distribution was divided into five groups (<15 ms, 15–30 ms, 30–45 ms, 45–60 ms, and >60 ms). A quality factor was assigned to each of these groups (1.0, 0.5, 0.25, 0.125, and 0) to weight the travel time data during the tomographic inversion described below.

4.2. 1-D Velocity Model

[15] The travel time data were initially used to develop a 1-D velocity model. The objective was to find a simple starting model that predicts the observed travel time data as accurately as possible, to fulfill the assumption of a local linearization of the inverse problem used in the subsequent 2-D tomography. A model description with only two parameters was chosen as a starting point: (1) a constant velocity at the surface and (2) a constant vertical velocity gradient. To determine the pair of parameter values that best explain the travel time data, a systematic scan of the parameter space was carried out using forward modeling and prediction error analysis [Bauer *et al.*, 2003]. For a given surface velocity and vertical gradient, the theoretical travel times were calculated using ray tracing methods [Zelt and Smith, 1992], and the RMS misfit between the observed and calculated travel time data was determined. The application of this

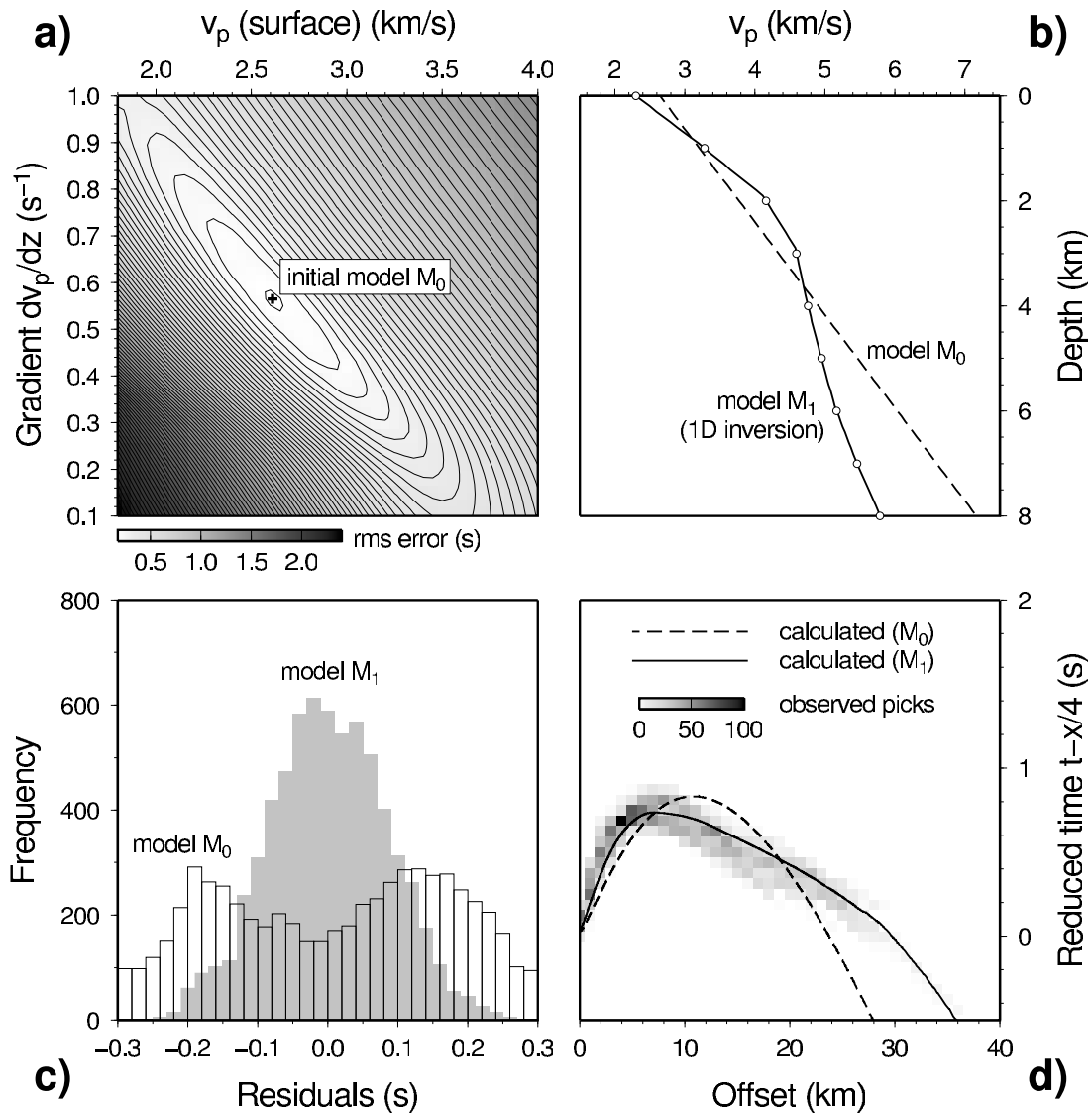


Figure 6. Determination of a starting model for the 2-D tomographic inversion using 1-D forward modeling and 1-D inversion. (a) A model description with two parameters (surface velocity, vertical velocity gradient) is assumed, and the prediction error function is determined by a systematic scan of the parameter space and corresponding forward calculations. (b) The best model M_0 serves as the initial model for the 1-D inversion, from which model M_1 was derived. (c) Histogram plot of the travel time residuals for the models M_0 and M_1 . (d) Comparison of observed and calculated travel times as a function of the source receiver offset (plotted with 4 km/s reduction velocity).

procedure for a reasonable range of values for both model parameters provided the RMS misfit function plotted in Figure 6a. The smooth error function exhibits a unique global minimum that defines the best model M_0 for this simple two-parameter problem.

[16] The model M_0 was then sampled at 1 km depth intervals (dashed line in Figure 6b). This 1-D function described by nine velocity values was further optimized using a damped least squares inversion algorithm [Thurber, 1983]. As a result of the inversion, the RMS misfit between the observed and calculated travel times was further reduced from 170 ms for model M_0 to 88 ms for the final 1-D model M_1 . Figure 6c illustrates the distribution of the residuals for both models. The improvement of the data prediction from

model M_0 to M_1 is also obvious in the travel time versus offset plot in Figure 6d. Although the two-parameter model M_0 gives a good overall fit to the data, the model M_1 with 1-km depth intervals is able to adapt to the different branches of the travel time-offset distribution.

4.3. 2-D Tomography

[17] The 1-D velocity structure (model M_1) served as the starting model for the 2-D tomographic inversion using the SIMUL2000 package [Thurber, 1983, 1993; Eberhart-Phillips, 1993]. The method is based on pseudo-bended ray tracing and a damped least squares inversion algorithm. Optimal damping of the inversion was determined by testing, on the basis of the trade-off criterion, which balances

between the minimization of the travel time RMS misfit and the variance of the velocity model perturbations [e.g., *Evans et al.*, 1994]. Data weighting during the inversion was calculated on the basis of the travel time uncertainties from repeated picking and the subdivision of the error histogram (Figure 5).

[18] The development of the velocity model was carried out in a graded inversion approach [e.g., *Evans et al.*, 1994], where the number of grid nodes defining the velocity model was systematically increased during the inversion process. Initially, the model M_1 was sampled at 4 km horizontal and 1 km vertical grid spacing. The modification of the initial model by the first inversion with five iterations is shown in Figures 7a and 7b. In this step, the RMS misfit was reduced from 88 to 66 ms. The node spacing was then further decreased after each five iterations using grid spacing of 2.0×0.5 km, 1.6×0.4 km, and finally 0.8×0.2 km (Figures 7c–7e, respectively). The RMS misfit was reduced at these stages to 44 ms, 38 ms, and 33 ms, respectively. An overview of the residual distribution for all data and each of the inversion stages is given in Figure 8, both in a histogram plot (left column) and as a function of the source and receiver location for each trace (right column).

[19] Figure 7 reveals how the major structures are established during the first iterations, as well as how these features are modified in the later fine-tuning phase of the inversion process. Another presentation of this development of the model is given in Figure 9, where the vertical velocity gradient for the models shown in Figures 7 is plotted. The vertical gradient of the P velocity is well suited to divide the generally smooth tomogram into subdomains of geological meaning [e.g., *Bauer et al.*, 2003]. The vertical gradient reveals a layered structure which is not obvious in the velocity tomograms in Figure 7. This can be used for a cross check when the smooth velocity model is correlated with borehole data and seismic reflection marker horizons. The models shown in Figures 7 and 9 are clipped where the resolution was lower than a given threshold value (for details, see next section).

4.4. Resolution Tests

[20] Resolution analysis was carried out to evaluate the reliability of the derived velocity model. Checkerboard tests included the reconstruction of given anomaly patterns to evaluate the spatial resolution across the tomographic section. For this purpose, the starting model M_1 of the 2-D tomographic inversion (Figure 7a) was superimposed with 10% sinusoidal velocity perturbations. Synthetic data were calculated for the real source and receiver configuration of the I-GET experiment using ray tracing methods [*Thurber*, 1983]. Gaussian noise was then added to the theoretical travel times with a standard deviation of 25 ms. This value was chosen for simplicity as a representative average for the error distribution derived from the repeated picking analysis (Figure 5).

[21] Three tests were run with different block sizes for the alternating anomaly patterns: 2×0.4 km, 5×1 km, and 10×2 km (Figures 10a, 10b, and 10c, respectively). The aspect ratio for the blocks corresponds to the horizontal/vertical dimensions of the tomographic section (40×8 km). The recovery of the models after the inversion is shown in Figures 10a–10c. As expected, the checkerboard pattern can

be reconstructed better in the upper parts than at greater depth, and the resolving capability decreases with decreasing block size. *Zelt* [1998] introduced a method to derive the lateral resolution from a series of checkerboard tests with different cell sizes using a semblance measure between the original and the recovered checkerboard models. As an alternative, the results of the checkerboard tests are here considered together with the spread values from the model resolution matrix (MRM) [*Toomey and Foulger*, 1989] to determine the model region with acceptable resolution [*Bauer et al.*, 2003]. Following the definition of *Micheline and McEvilly* [1991], the spread value s_j for a model node j is derived by analysis of the elements r_{kj} of the corresponding row of the MRM using the following equation:

$$s_j = \log \left(\|\vec{r}_j\|^{-1} \sum_{k=1}^N \left(\frac{r_{kj}}{\|\vec{r}_j\|} \right)^2 D_{jk} \right), \quad (3)$$

where \vec{r}_j is the averaging vector of the j th model parameter and D_{jk} measures the distances between the model nodes considered. The spread value describes the sensitivity of a model parameter and its dependency on the surrounding model nodes. Low values indicate high resolution and less smearing of information to adjacent nodes. On the basis of the recovery of the checkerboard models, a spread value of 4.8 was chosen to clip the tomographic models as presented in Figures 7 and 9.

5. Velocity Model, Wide-angle Reflections, and Marker Horizons

[22] The results from the tomography were combined with information from industrial seismic reflection data available for the study area. Figure 11 shows six profiles which were measured by exploration companies between 1971 and 1990 and which have been reprocessed and reinterpreted to develop a 3-D geological model around the geothermal research well at Groß Schönebeck [*Moeck et al.*, 2009]. Because the data are proprietary, only the interpretations can be shown. The 3-D model was constructed on the basis of the six 2-D profiles and well data using the interpolation technique described in *Moeck et al.* [2009]. We used the same interpolation method to extract the marker horizons along the I-GET profile which crosses the 3-D geological model (Figure 11).

[23] A comparison with a seismic reflection image derived from the I-GET data would be useful to validate the interpolation of the marker horizons from the six industrial profiles. However, the I-GET experiment was designed for refraction tomography, and the acquisition parameters and frequency content of the wide-angle data are unsuitable for reflection processing in our case. Alternatively, prominent wide-angle reflections were modeled and compared with the interpolated marker horizons. For this purpose, the final velocity tomogram was converted to the model parameterization of RAYINVR [*Zelt and Smith*, 1992]. The travel times of wide-angle reflections W1 and W2 (see examples in Figures 12a and 13a) were determined for all shots, and corresponding reflectors were modeled using the ray-based forward and inverse modeling method of *Zelt and Smith* [1992]. The results show very good agreement between reflector W1 and marker horizon X1 representing the top of the Zechstein salt (Figure 12). W1 validates the interpolation

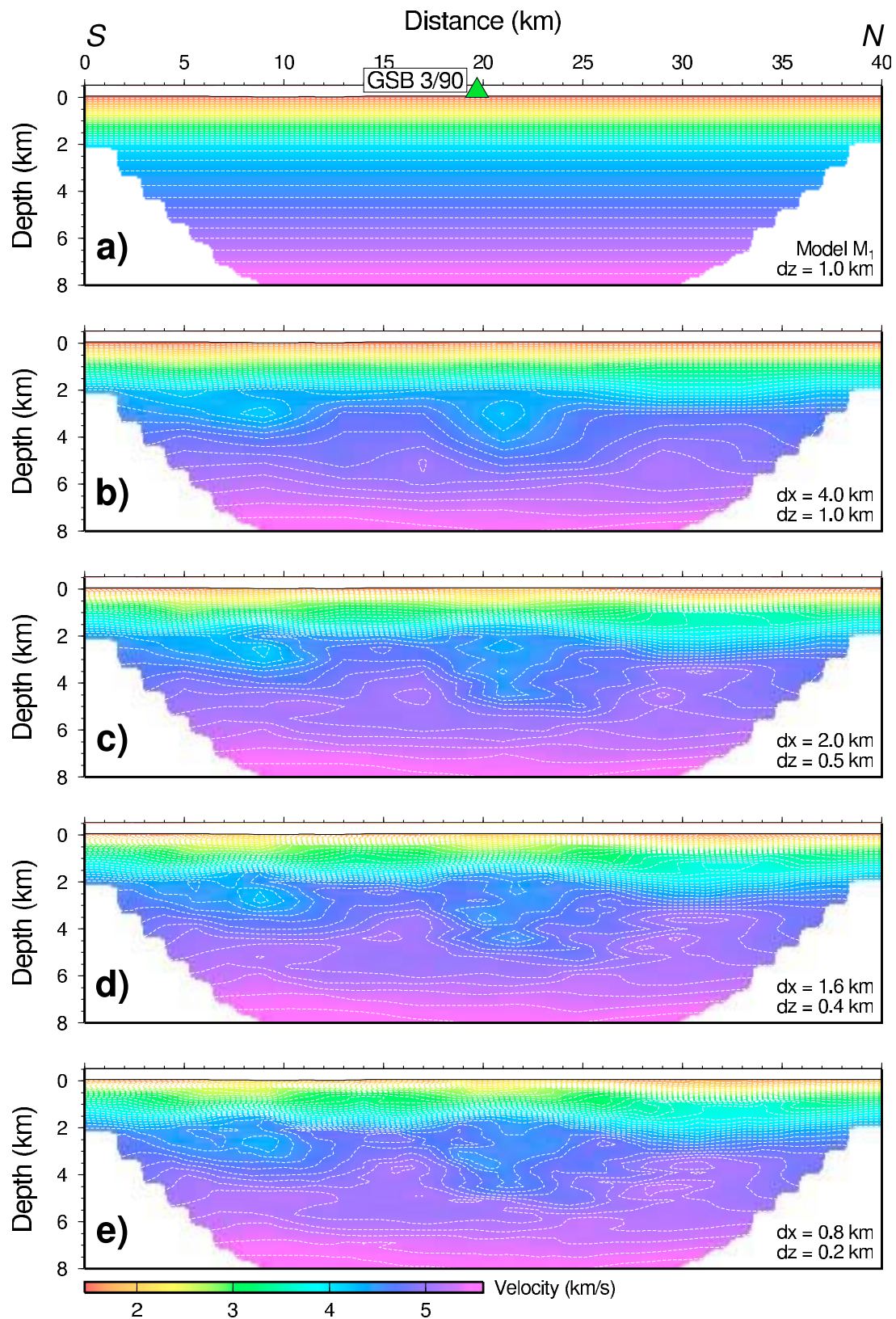


Figure 7. Development of a 2-D velocity model using a tomographic inversion algorithm. (a) The starting model corresponds to model M_1 as determined from 1-D inversion (see Figure 6). (c–e) A graded inversion approach was used whereby the horizontal and vertical spacing (dx and dz , respectively) of the tomographic grid were systematically decreased during the interactive inversion procedure. (e) The final 2-D velocity model. Contour lines correspond to 0.1 km/s isovelocity steps.

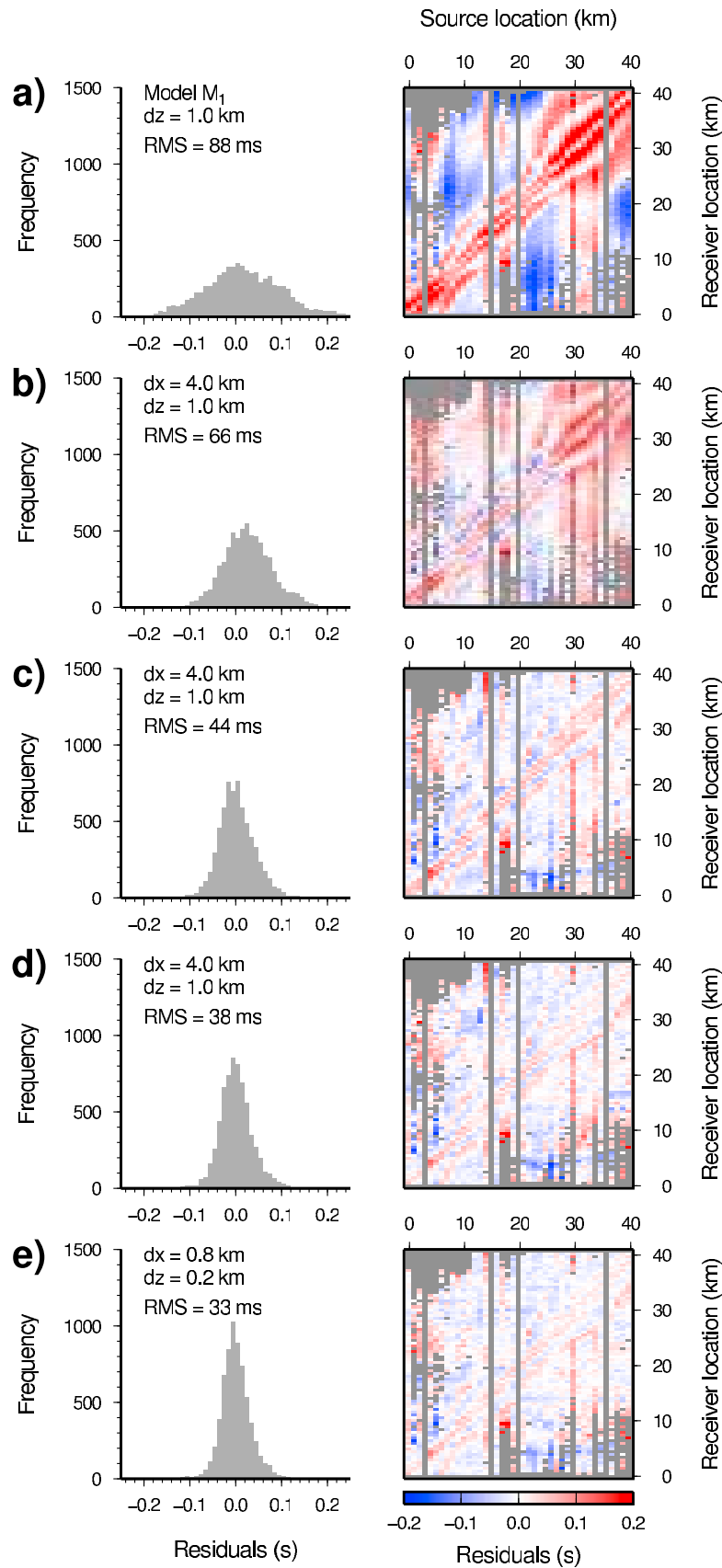


Figure 8. Changes in model prediction error for 2-D velocity models shown in Figures 7a–7e. The travel time residuals are presented as histogram distributions (left) and 2-D functions of the source and receiver locations (right).

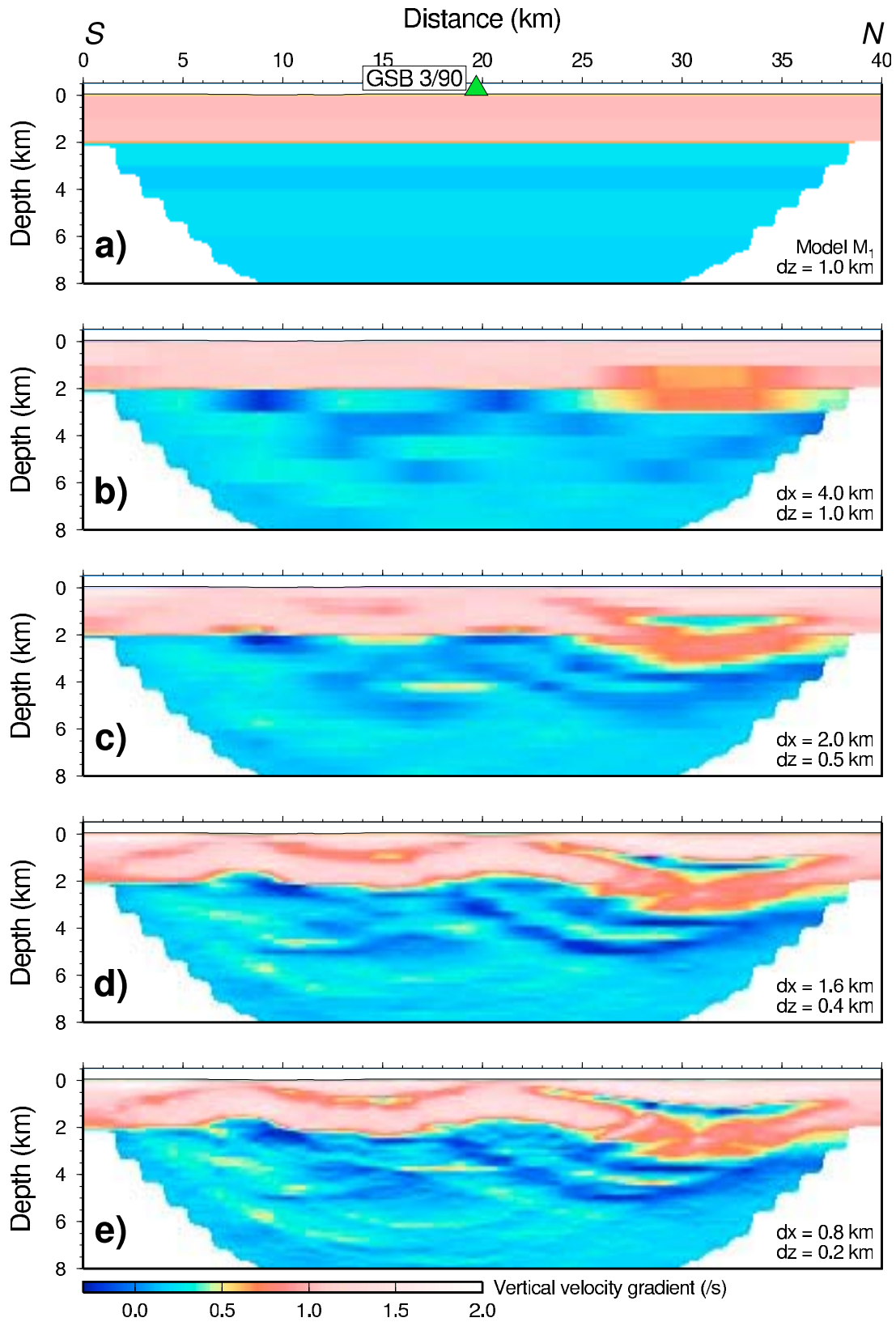


Figure 9. Vertical velocity gradient plotted for the 2-D velocity models shown in Figure 8. (a) The starting model corresponds to model M_1 derived by 1-D inversion (Figure 7). (b–e) The horizontal and vertical grid node spacing is decreased at several stages of the 2-D tomographic inversion procedure.

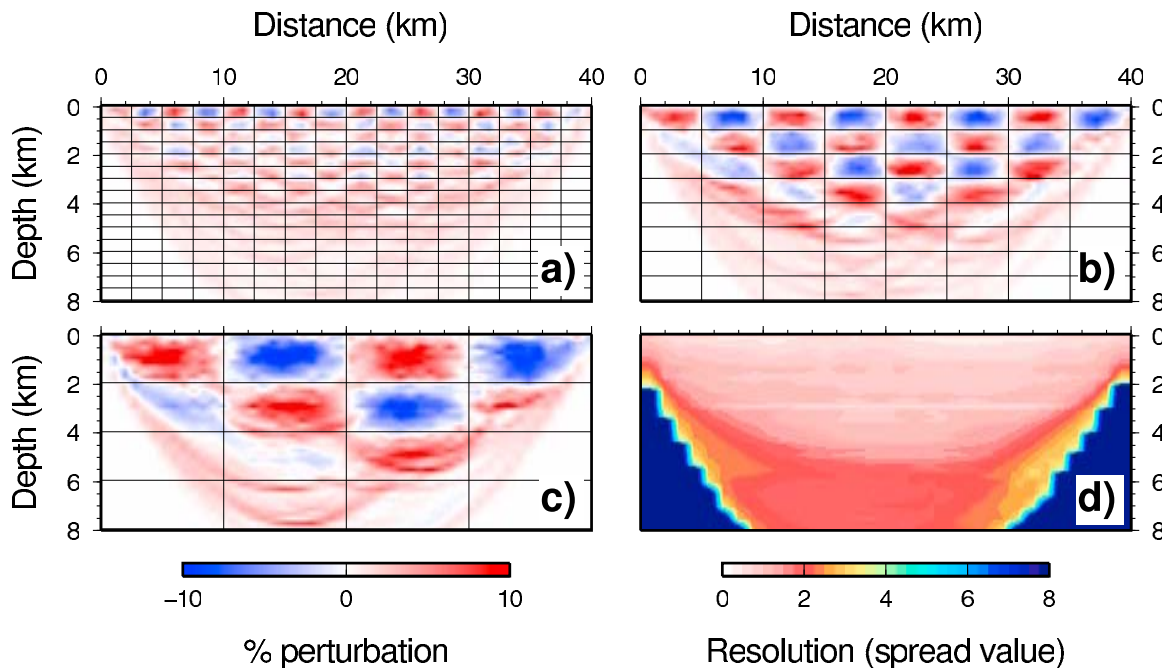


Figure 10. Resolution tests for the 2-D travel time tomography. Recovered anomalies for different checkerboard patterns (a) 2.5×1.0 km, (b) 5×1 km, (c) 10×2 km. To generate the input model, 10% velocity perturbations were added to the starting model used for the 2-D inversion (Figure 7a). (d) Distribution of the spread values derived from the resolution matrix. High resolution corresponds to low spread values.

of the marker horizon and allows additional tracking of the Zechstein top further to the south. On the basis of the ray coverage (Figure 12b), the wide-angle reflections W1 are not observed or less pronounced in the region of the salt pillows, suggesting a smaller velocity contrast compared with the salt lows. This is supported by the tomography results (Figure 12b). Wide-angle reflection W2 was modeled as a boundary at 4.7 to 5 km depth, where no marker horizons were determined. The latter is related with the general difficulty in imaging the section below the Zechstein salt (below Z1 in Figure 13b) using seismic reflection data. The wide-angle reflections are observed at distances beyond a typical industrial seismic reflection survey (Figure 13a) and thus allow for the detection of the sub-Zechstein boundary W2.

6. Interpretation and Discussion

[24] The final velocity model derived by the 2-D travel time tomography and the vertical gradient of this model are shown in Figure 14. Besides deep crustal seismic refraction experiments [e.g., Aichroth *et al.*, 1992; Schulze and Lück, 1992], only a few studies have investigated the internal sedimentary velocity structure in the central European basins so far. A velocity model along a seismic refraction profile near the I-GET study area was derived for the SW Baltic Sea [Bleibinhaus *et al.*, 1999]. Using larger source and receiver spacing and a longer profile length than in I-GET, the model extends over 200 km distance with a depth of penetration of 35 km, and the sedimentary part of the basin is resolved with less details in their models compared with the results from Groß Schönebeck. Another

regional tomographic velocity model derived by Nielsen *et al.* [2005] for the southeastern North Sea focused more on the sedimentary section, but the resolution was lower compared with the I-GET images because of their larger receiver spacing. A regional scale tomographic model of a geothermal reservoir could be determined for the Groß Schönebeck geothermal site because of the specific source and receiver geometries used in the I-GET experiment. From this perspective, the velocity and the vertical gradient models shown in Figure 14 provide new insights into the structure and the composition of the sedimentary section and extend the geological knowledge around the geothermal reservoir. In the following section, the results are discussed in terms of lithostratigraphic structure, their implications for the salt tectonic history, and their relationship to the temperature field on the basis of a thermal modeling approach.

6.1. Lithostratigraphy

[25] To relate the tomography results with the lithostratigraphic structure, the velocity model and the vertical gradient image are superimposed with the seismic marker horizons determined from the integration of existing seismic reflection profiles and well data (Figure 14). Marker horizons can be included only beyond profile distances of 15 km as the 3-D geological model overlaps only part of the I-GET profile. The relationship between marker horizons and lithostratigraphy at the geothermal well GrSk 3/90 is shown in Figure 15 and can be used to identify the expression of the sedimentary structure in the tomographic model. The velocity distribution reflects the layered structure traced by the marker horizons. This becomes even more obvious in the

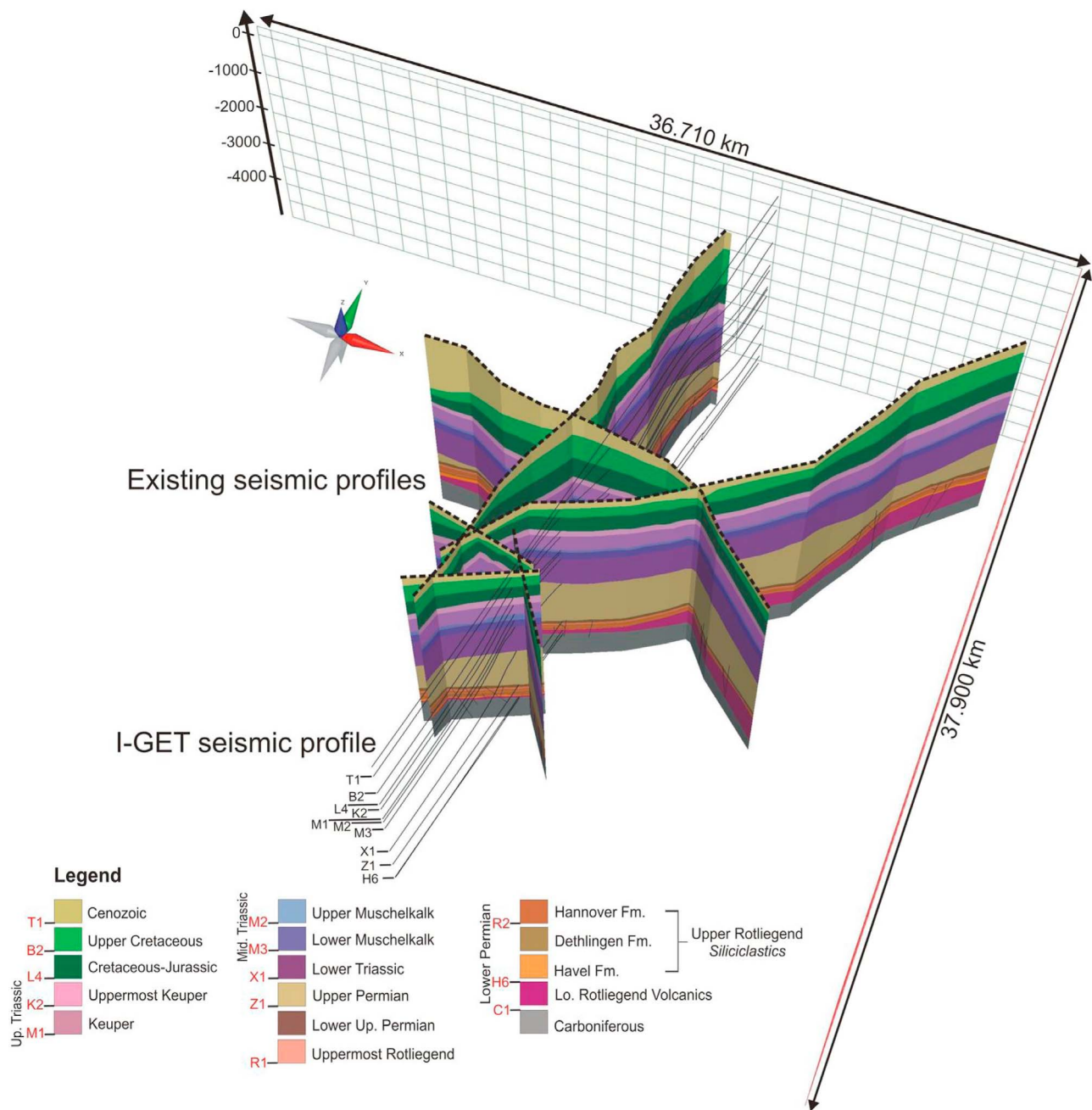


Figure 11. Interpretation of existing industrial seismic profiles in the study area [Moeck *et al.*, 2009]. Layers are color-coded corresponding to the legend with lithostratigraphy. Marker horizons were interpolated along the I-GET seismic profile using the method described by Moeck *et al.* [2009].

vertical gradient presentation (Figure 14b). The velocity and vertical gradient model, to the first order, can be divided into three major sections: (1) Cenozoic to Muschelkalk, (2) Buntsandstein, Zechstein, Rotliegend, and (3) Pre-Permian. These are discussed in the following subsections.

6.1.1. Cenozoic to Muschelkalk

[26] The upper part from the Cenozoic down to the base of Muschelkalk (marker horizon M3) is characterized by a strong increase in velocities from 1.8 km/s to 4 km/s, which is most likely related to mechanical compaction by overburden pressure. The large velocity increase is only interrupted in the Jurassic (Lias) between marker horizons B2

and L4, where the gradient gets much smaller (at well GrSk; Figure 15c) or negative (at 25 km–35 km distance in Figure 14b). The lithology in the Lower Jurassic in the NEGB is dominated by marine shales and sandstones. The smaller vertical velocity gradient indicates different properties of these strata in terms of mechanical compaction effects compared with the surrounding rocks. For the seismic tomography interpretation, the vertical gradient structure down to M3 can be used to trace the corresponding seismic reflector. As indicated in Figure 14b, marker horizons B2, L4, and M3 can be interpreted in the southern part

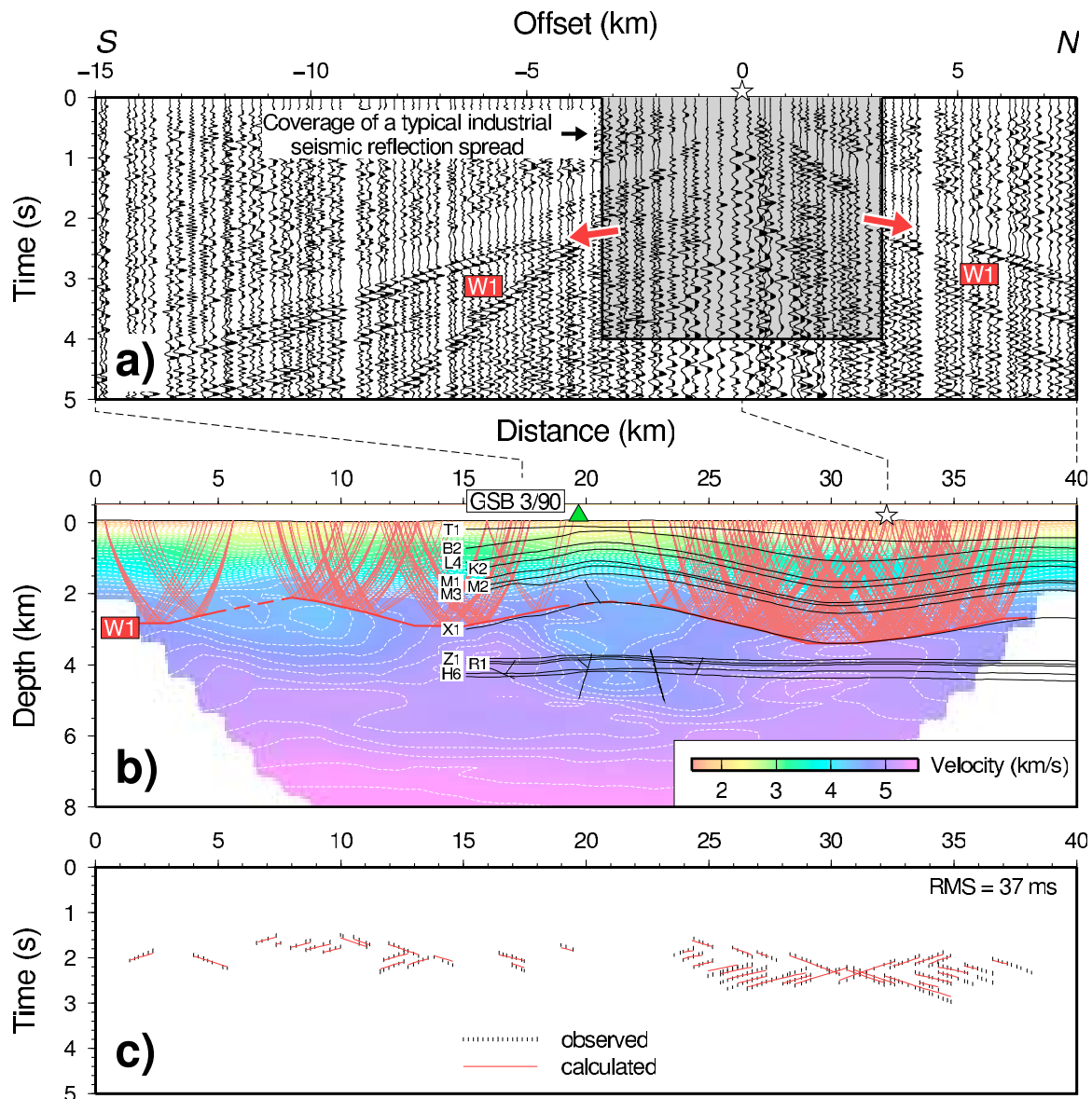


Figure 12. Modeling of wide-angle reflections observed along the I-GET profile. (a) Example of shot-gathered data showing prominent wide-angle reflections W1. Shaded area indicates coverage of a typical industrial seismic reflection spread. (b) Reflector W1 determined by ray-based forward and inverse modeling of travel time data from all shots using the method of Zelt and Smith [1992]. Superimposed are marker horizons interpolated from existing industrial seismic profiles [Moeck *et al.*, 2009] as shown in Figure 11. (c) Observed and calculated travel times.

of the profile where no reliable control from preexisting seismic reflection data exists.

6.1.2. Buntsandstein, Zechstein, Rotliegend

[27] The section between M3 (top Buntsandstein) and C1 (base Permo-Carboniferous volcanic rocks) exhibits velocities between 4 km/s and 5 km/s, with much smaller vertical gradients compared with the overburden (Figure 14). The change to a smaller velocity increase with depth below 2–3 km is a typical range for the transition from mechanical to chemical dominated compaction [e.g., Ramm, 1992]. The velocities of the Buntsandstein, the Zechstein evaporites, and the Rotliegend sandstones and the Permo-Carboniferous

volcanic rocks are similar, but the layers can partly be distinguished on the basis of the shape of the isovelocities in Figure 14a. The interface between Zechstein and Rotliegend shows a stronger positive velocity gradient between 15 km and 20 km in Figure 14b, suggesting a sharp velocity contrast between these strata. The velocity distribution reveals lateral variations within the layers which reflect a lithological heterogeneity not expected from the continuous appearance of the seismic reflection marker horizons. This variability is discussed in section 6.2 in relation to the salt tectonic processes.

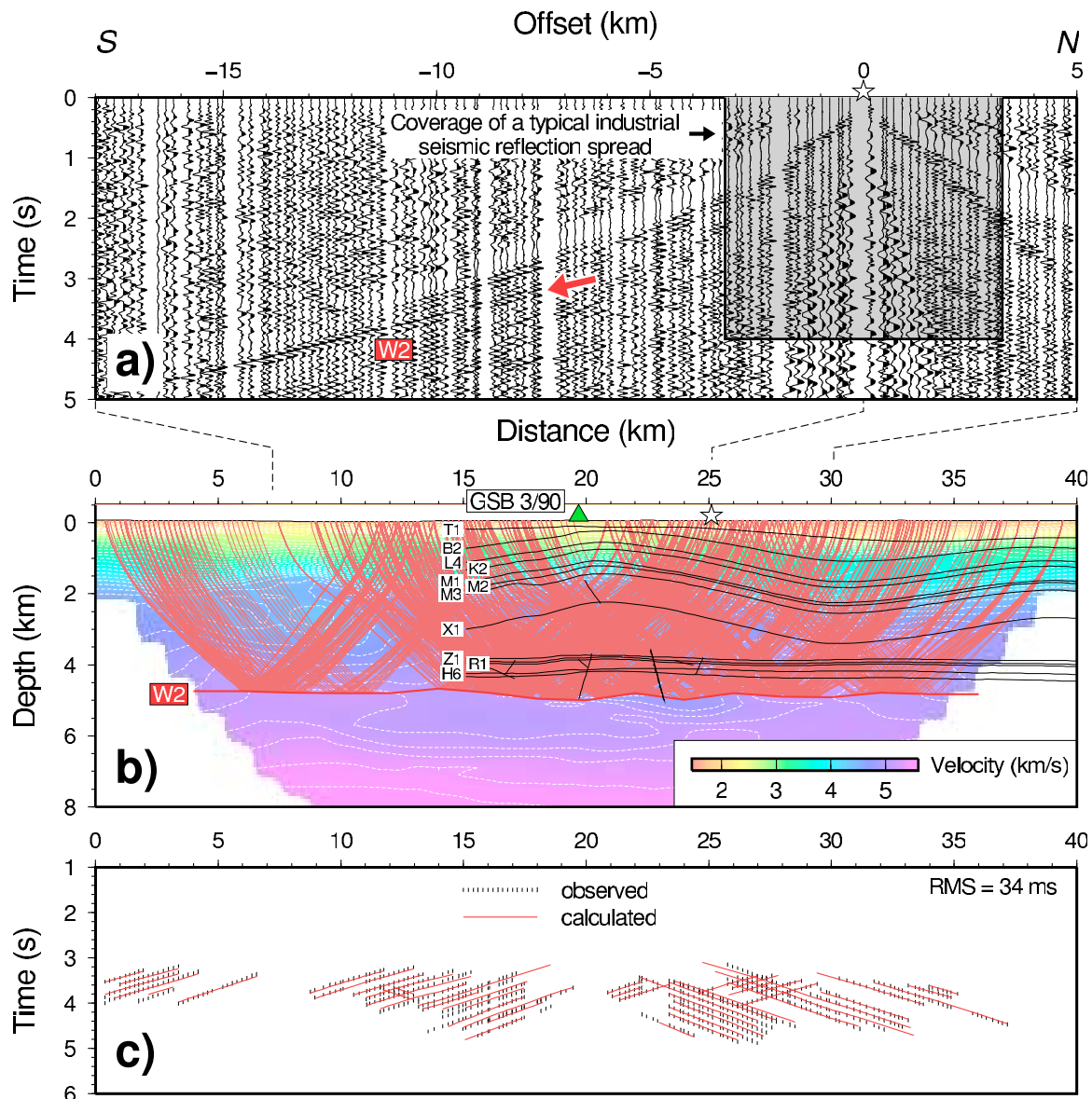


Figure 13. Modeling of wide-angle reflections observed along the I-GET profile. (a) Example of shot-gathered data showing prominent wide-angle reflections W1. Shaded area indicates coverage of a typical industrial seismic reflection spread. (b) Reflector W2 determined by ray-based forward and inverse modeling of travel time data from all shots using the method of Zelt and Smith [1992]. Superimposed are marker horizons interpolated from existing industrial seismic profiles [Moeck *et al.*, 2009] as shown in Figure 11. (c) Observed and calculated travel times.

6.1.3. Pre-Permian

[28] The deepest part of the model resolved is characterized by velocities of 5 km/s to 5.5 km/s. Boundary W2 at 4.7 to 5 km depth was derived by modeling of wide-angle reflections and is interpreted as the top of the Pre-Permian in agreement with Franke *et al.* [1989]. A subvertical feature with lower velocities is imaged below C1 at 21.5 km profile distance and is interpreted as a deep fault in the lowermost Rotliegend and uppermost Pre-Permian. The relevance of this structure for the salt tectonic history and the geomechanical conditions in the geothermal reservoir is discussed below. The boundary between the Paleozoic and the crystalline basement (>6 km/s) is not resolved, as it is expected

for the North German Basin at depths >9 – 10 km [e.g., Aichroth *et al.*, 1992; Schulze and Lück, 1992].

6.2. Salt Tectonics

[29] Salt tectonics have a major impact on the mechanical conditions at the Lower Rotliegend geothermal reservoir. The deformation due to salt movements is imaged in the tomographic section in Figure 14. The vertical gradient structure and the shape of boundary W1 reflect the deformation of the Triassic to Tertiary strata related to the upwelling of three salt pillows along the profile. Of note is that the southernmost pillow (5 km to 10 km distances in Figure 14b) was not known from preexisting seismic reflec-

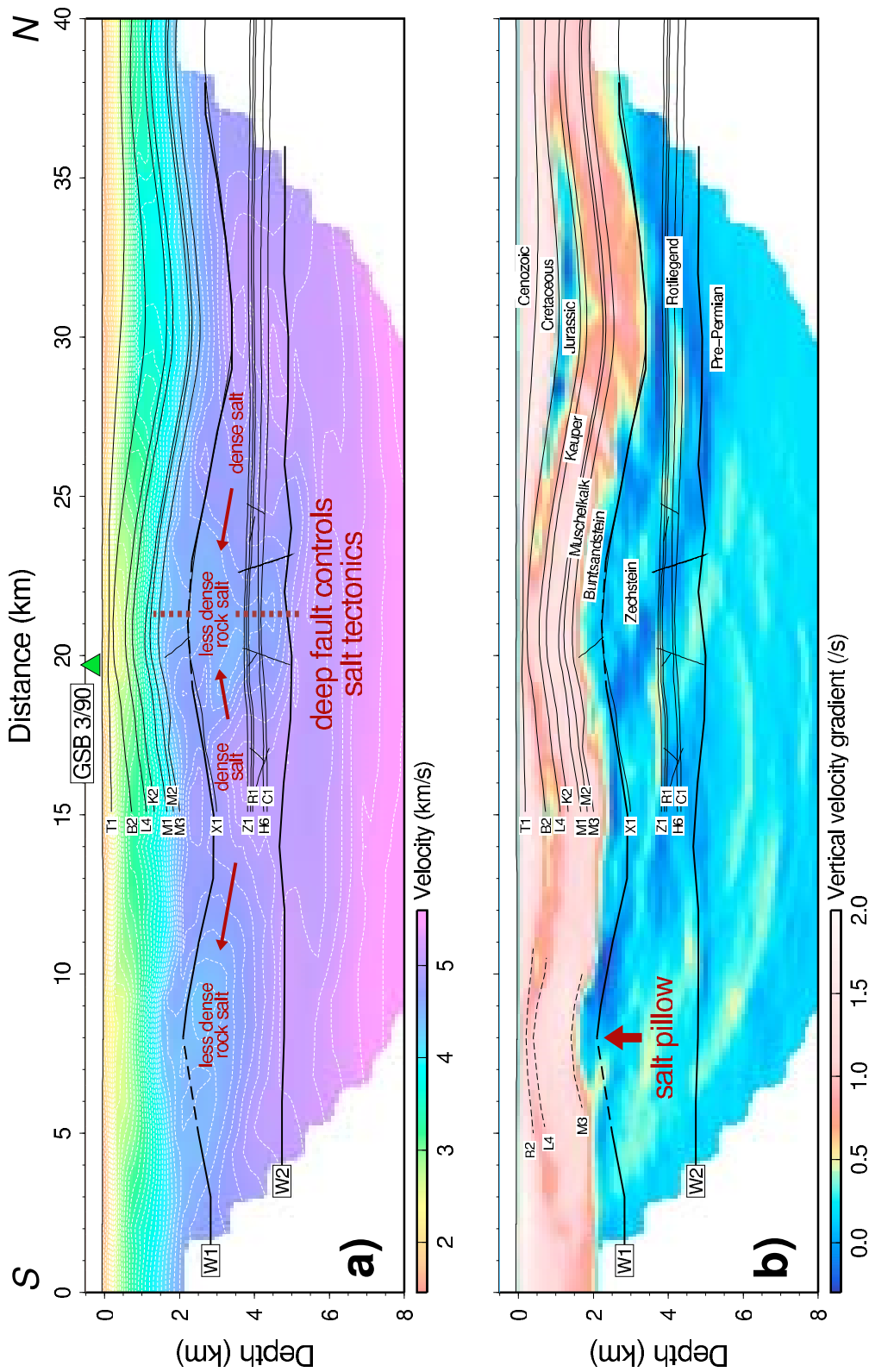


Figure 14. Final velocity and vertical gradient models from tomographic inversion. (a) P wave velocity model overlaid with 0.1 km/s isovelocity contours (dashed white lines). Superimposed are marker horizons and faults from existing seismic reflection data [Moeck *et al.*, 2009], boundaries W1 and W2 from modeling of wide-angle reflections as shown in Figures 12 and 13, and interpreted lithology. The location of well GrSk 3/90 is indicated by the green triangle. (b) Vertical velocity gradient with marker horizons, boundaries W1 and W2, and stratigraphic units. Dashed lines indicate determination of marker horizons using the velocity gradient structure. A new salt pillow is interpreted at distances between 5 km and 10 km.

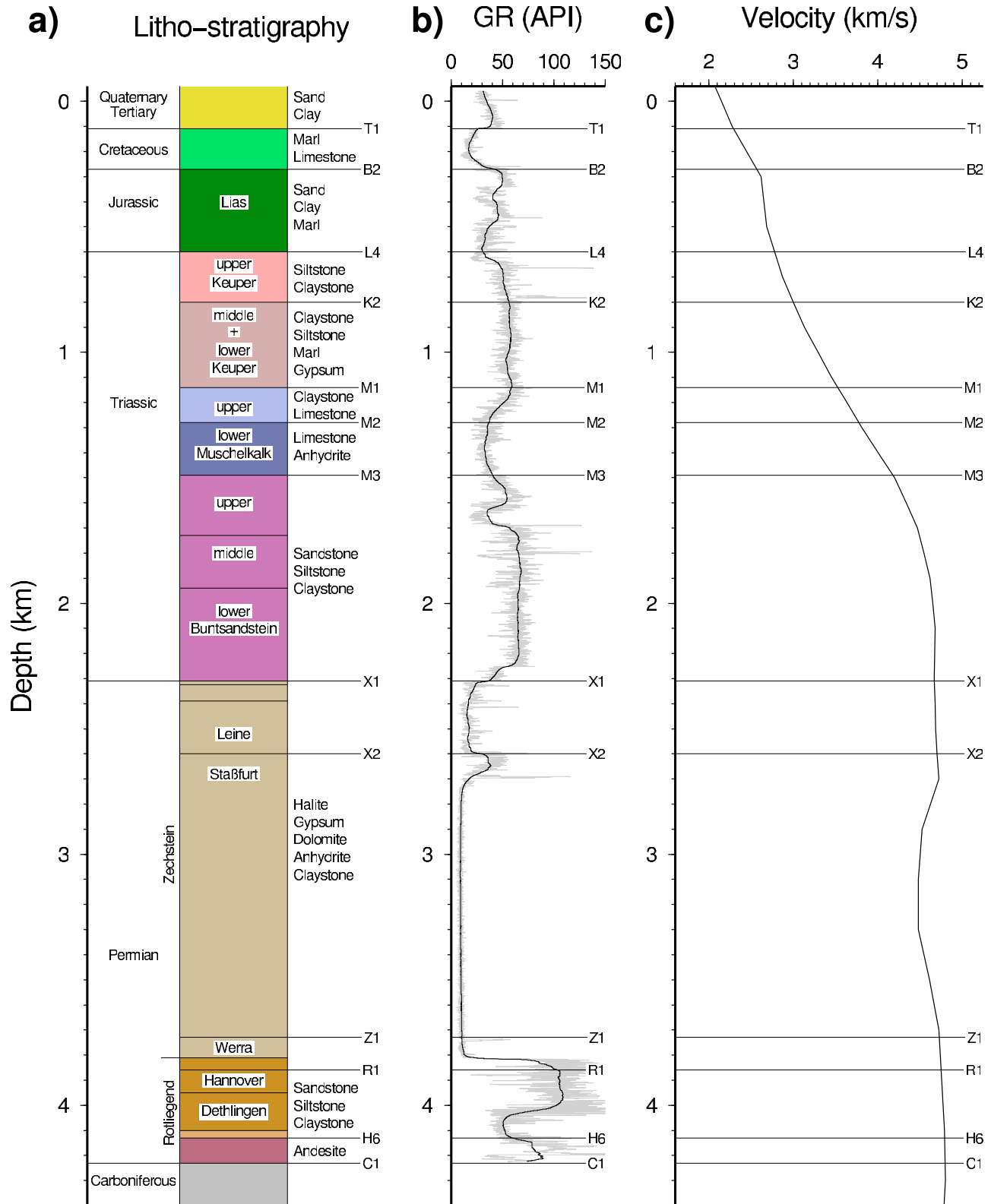


Figure 15. (a) Lithostratigraphic units at well GrSk 3/90 and seismic reflection marker horizons [Moeck *et al.*, 2009]. (b) γ -ray log (shaded line unfiltered, black line low-pass-filtered) and marker horizons, (c) P wave velocity profile extracted from the tomographic model shown in Figure 11a and marker horizons.

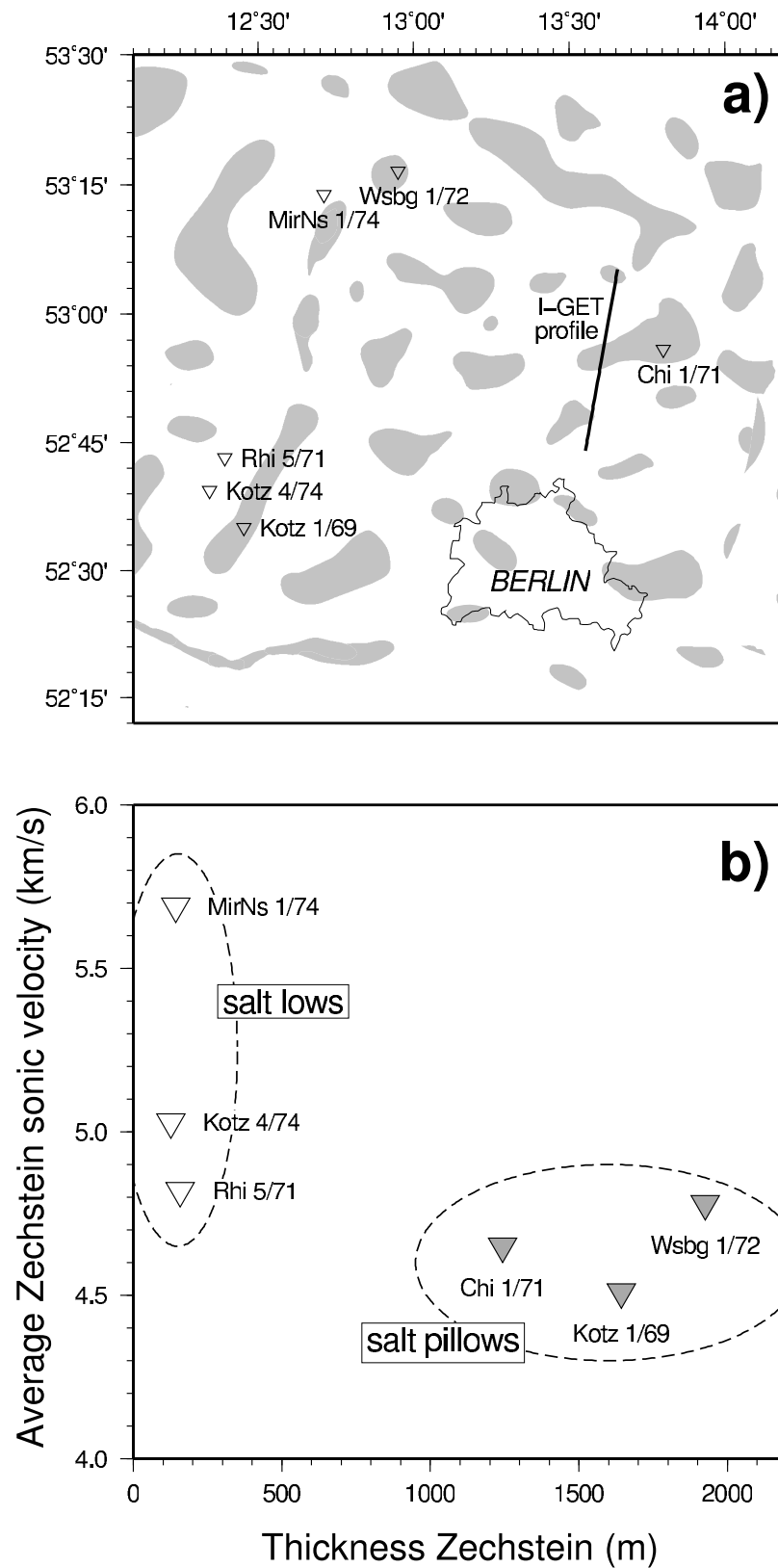


Figure 16. (a) Distribution of salt pillows in the Northeast German Basin (after Reinhold *et al.* [2008] and Moeck *et al.* [2009]). I-GET seismic profile is drawn as black line. Triangles mark locations of deep research wells with available sonic velocity logs within the Zechstein salt [Hoth *et al.*, 1993]. (b) Sonic velocity averaged for Zechstein interval as a function of Zechstein thickness. The location of the six deep research wells analyzed is shown in Figure 16a.

tion data and was identified only by the I-GET results. The salt pillows are characterized by lower velocity values of 4.5 km/s to 4.7 km/s compared with velocities of 4.8 km/s to 5.1 km/s in the salt lows between the upwelling features. This pattern was not previously known and was not expected from the continuous appearance of the seismic reflection data. To validate this new observation, we analyzed sonic logs from deep research wells available for the study area (Figure 16). We determined the average velocity within the Zechstein layer as interpreted by *Hoth et al.* [1993] and plotted this average value against the thickness of the Zechstein layer (Figure 16b). The results support the interpretation of the pattern in the tomographic section, with a general decrease of the average velocity in the thick salt pillows compared with the thin salt lows.

[30] One possible explanation of the velocity pattern is that less dense components of the salt matrix were mobilized and denser material remained in the salt lows during the formation of the salt pillows and the related dynamic processes (Figure 14a). The explanation of the velocity variations by such lithological differentiation agrees with the velocity range of 4.5 to 5.2 km/s reported for rock salt [e.g., *Schoen*, 1996]. Furthermore, the reduction in velocity under the upwelling regions could partly be related to enhanced deformation and strain accompanied by an increase in microfracture density. This is supported by an observation of *Popp and Kern* [1998], who found a velocity decrease of almost 0.2 km/s due to an increase in permeability on the basis of borehole measurements in a salt rock structure. Increased strain and related mechanical weakness could also be responsible for the reduction in velocity within the Buntsandstein (M3 to X1) directly above the salt pillow (e.g., ~21 km and ~8 km distance in Figure 14a). The absence of an equivalent velocity reduction above M3 could then be due to the change from mechanical to chemical compaction and the related change in the rheological behavior as deduced from the vertical gradient.

[31] Below the central salt pillow close to the GrSk 3/90 borehole, a subvertical feature is imaged at depths between 3.5 km and 4.5 km crossing parts of the lowermost Zechstein, Rotliegend, and uppermost Pre-Permian. The structure is interpreted as the trace of a regional deep fault trending approximately WNW-SSE (Figure 2). This interpretation is in agreement with the fault-bounded graben structure around the subvertical low-velocity feature drawn in Figure 14a on the basis of preexisting seismic reflection data [*Moeck et al.*, 2009]. The shape of boundary W2 determined from wide-angle reflections (Figure 13) supports the fault interpretation. The coincidence of the salt pillow and the deep fault suggests that at this particular place, the location of the salt movement was influenced by the preexisting weakness zone of the deep fault structure. For the Rotliegend reservoir layer, it can be concluded that the mechanical conditions are optimal for geothermal stimulation under the salt pillow and fractures could be used along the strike of the deep fault and the graben structure.

6.3. Modeling of Possible Temperature Effects on Seismic Velocity

[32] Lateral velocity variations observed particularly in the salt layer were discussed in the previous section in terms

Table 1. Thermal Parameters Applied in the Modeling^a

Horizon	Layer No.	λ [W/m/K]	A [μ W/m ³]	v_p [km/s]
Base	1	2.7	1.4	5.5
TKarb-TRotl	2	3	1.4	5.1
Z1-TRotl	3	4.5	0.4	5
Z1-X1	4	4.5	0.4	4.9
X1-M3	5	2.3	1.8	4.7
M3-M2	6	2	1	4.4
M2-K2	7	2.7	1.1	4.1
K2-L4	8	2.8	1.5	3.85
L4-B2	9	2	1.55	3.75
B2-T1	10	2	0.6	3.1
T1-Top Quaternary	11	1.8	1.1	2.1

^aThermal conductivity (λ) is given for room conditions and was corrected for temperature using the formula of *Somerton* [1992]. λ and radiogenic heat production (A) are based on values given by *Norden and Förster* [2006] and *Norden et al.* [2008].

of lithological and rheological heterogeneity related to salt mobilization. Owing to the high thermal conductivity contrast between rock salt (~4.5 W/m/K) and surrounding rocks (~2–3 W/m/K), heat refraction occurs, altering the thermal field. To quantify the degree by which seismic *P* wave velocities could be affected by local thermal anomalies, thermal modeling was conducted.

[33] Modeling was performed on the basis of the finite-elements approach using the partial differential equation (PDE) toolbox of the commercial software MATLAB 7.0.4. Here, the following equation for 2-D steady-state heat conduction:

$$\frac{\partial}{\partial x} \left(\lambda(x, z) \frac{\partial T(x, z)}{\partial x} \right) + \frac{\partial}{\partial z} \left(\lambda(x, z) \frac{\partial T(x, z)}{\partial z} \right) = -A(x, z), \quad (4)$$

with A the internal heat production and $\lambda(x, z)$ the thermal conductivity of the rock (both are assumed to be isotropic) is solved numerically. Thereby the temperature distribution $T(x, z)$ within the model (with x the horizontal coordinate and z the vertical coordinate) is determined by the temperature-dependent thermal conductivity distribution $\lambda(x, z)$, the heat production distribution $A(x, z)$, and the appropriate thermal boundary conditions. On the basis of the geological model, 11 model layers have been considered and parameterized for thermal conductivity and radiogenic heat production (Table 1), whereby the lowermost layer represents a virtual pre-Permian layer to a depth of 10 km. The thermal conductivity of the rocks was corrected for temperature using the formula of *Somerton* [1992]. The finite-element mesh size is variable according to the different size of the model layers. Polygons representing relatively thin sedimentary formations have a maximum mesh size of about 200×200 m, and those representing thicker formations have a mesh size of up to 400×400 m. In the modeling, a constant surface temperature of 9°C is used. For the lower boundary condition at 10 km, a constant heat flow of 55 mW/m² was used on the basis of the determined surface heat flow of the NEGB (77 mW/m²) [*Norden et al.*, 2008]. At the side boundaries of the 2-D models, horizontal temperature gradients are assumed to be zero (no horizontal heat transfer).

[34] First, a simplified 2-D conductive thermal model along the I-GET section was set up (Table 1). In this model, all strata were assumed to be layered horizontally. From this

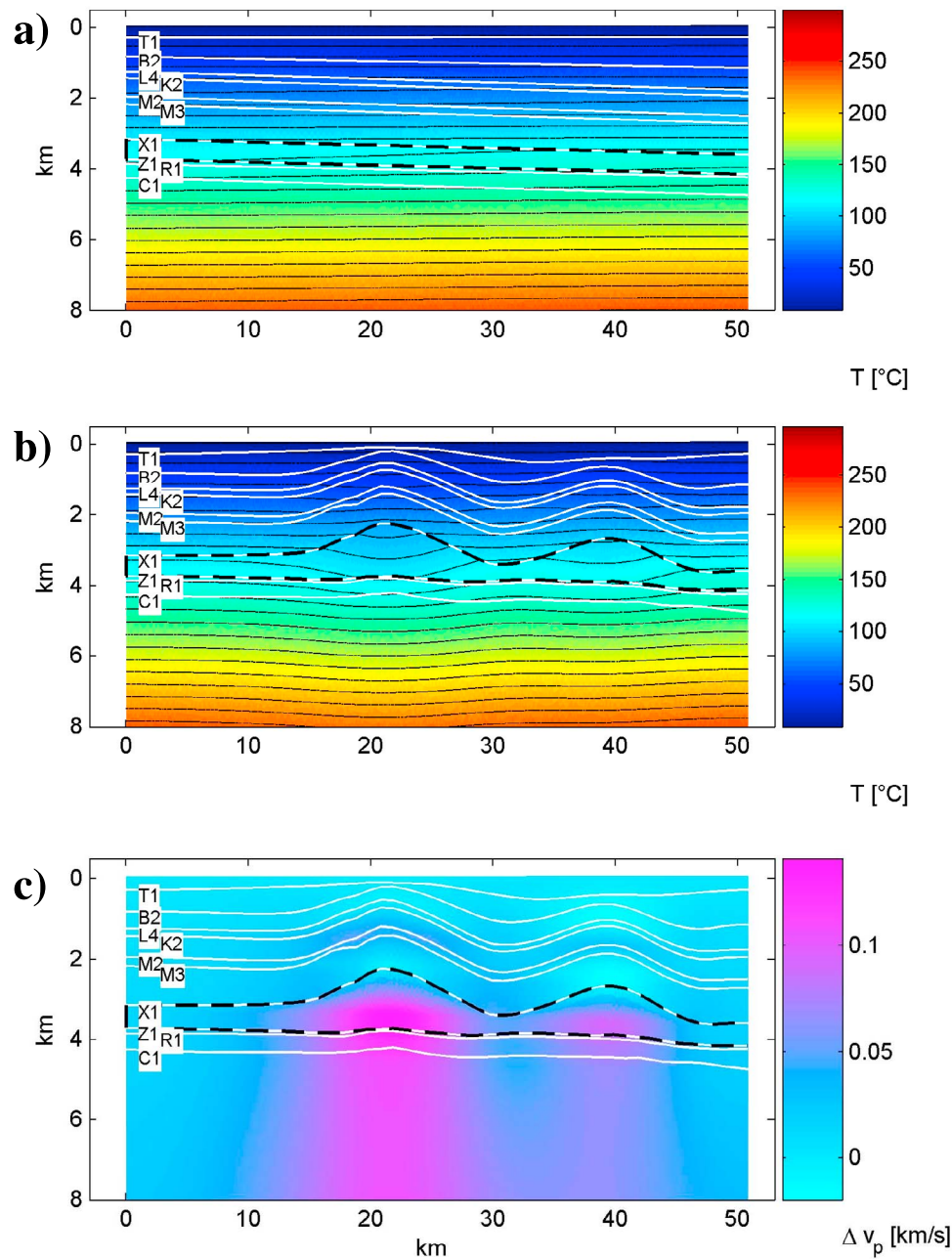


Figure 17. Results of thermal modeling and estimation of temperature effects on seismic velocity. (a) Temperature field for a subhorizontally layered sedimentary succession without salt tectonics. (b) Modification of the temperature field by formation of salt pillows. The difference between Figures 17a and 17b provides the temperature anomaly related to the evaporite mobilization. (c) Possible changes in P wave velocity caused by the change in temperature.

model, a baseline temperature field was calculated (Figure 17a). To estimate the temperature anomaly ΔT due to the salt pillow structure, the temperature field of a second model, now considering the sedimentary layers modified by salt tectonics, was calculated (Figure 17b). The anomaly in the temperature field (ΔT) was then used to estimate the corresponding effect in the P wave velocity field. Seismic velocity and temperature are related empirically by a nearly linear anticorrelation for most rock types [e.g., Schoen, 1996]. By assuming a steepest possible slope of dv_p/dT of -0.01 km/s/°C [e.g., Schoen,

1996], the maximum changes of P wave velocities due to changes of the temperature field can be estimated and calculated for the model (Figure 17c).

[35] The thermal modeling reveals that temperatures directly above the salt pillow are increased by about 2–4°C but lowered by almost 14°C in and below the salt structure. This temperature field is related to the thermal chimney effect of the highly conductive salt. Owing to the effect, the P velocity could show an increase of up to 0.14 km/s in the salt. This, however, is opposite to the observed decrease

in velocity within the salt pillow. The same holds for the Rotliegend reservoir underneath. It must be concluded that the lithological and rheological differences between salt lows and pillows must be even larger than assumed to compensate for the effects related to the temperature variations estimated for the cross section.

7. Conclusions

[36] A seismic refraction experiment was conducted to allow for the tomographic velocity imaging at a regional to geothermal reservoir scale. The spatial resolution achieved is higher than during previous studies in the North German Basin because of denser source and receiver spacing that were focused on a geothermal well. The results provide new insights into the structure and composition of the sedimentary section down to the Pre-Permian and complement the structural picture deduced from existing seismic reflection data.

[37] The vertical gradient of the P velocity is particularly suited to reflect the layered lithostratigraphic structure. A generally strong vertical velocity increase above the top Buntsandstein (marker horizon M3) is related to mechanical compaction effects, with the exception of the Lower Jurassic, which shows smaller or negative vertical gradient values indicating distinct mechanical compaction behavior. Below M3, a change to generally small vertical gradients is observed, indicating that mechanical compaction is finished. This can be explained by the effects of cementation and chemical compaction of the pore space starting at such depths, which result in a general stabilization of the grain matrix (e.g., Ramm [1992]). Hence, we interpret this change to small vertical velocity gradients as the transition from mechanical to chemical compaction. Several marker horizons (B2, L4, M3) could be identified in regions without seismic reflection control using the characteristic vertical velocity gradient pattern. The gradient image allows the effects of salt tectonics to be inferred whereby a new salt pillow is interpreted in the southern part of the model.

[38] The Zechstein salt layer shows a characteristic velocity distribution not previously known, with higher velocities around salt lows and decreased velocities within the salt pillows. These velocity variations could reflect the movement of less dense salt components into the upwelling pillows, with denser salt remaining in the salt lows. The velocity reduction could also be due to increased strain and fracture density in the upwelling region. A subvertical low-velocity feature was imaged in the Pre-Permian directly under the salt pillow closest to well GrSk 3/90. The interpreted deep fault is trending WNW-ESE [Katzung, 1990] and is related to a fault-bounded graben in the Lower Rotliegend level [Moeck et al., 2009]. At this location, the mechanical conditions should be optimal for extraction of geothermal energy from the Rotliegend sandstones and volcanic rocks. Fractures parallel to the direction of the Pre-Permian fault and the graben should be used for fluid circulation.

[39] Thermal modeling was carried out to predict possible effects of temperature variations at salt structures on the seismic velocity structure. On the basis of the modeling, it is assumed that the variations within salt structures regarding density (lithology) and rheology (microfracture density) have to be larger than the temperature-related increase of P velocity

to produce the observed effect of a velocity decrease within the salt pillow.

[40] The thermal and mechanical conditions in the Rotliegend reservoir related to salt pillows and salt lows in the overlying Zechstein are open issues for further research to optimize geothermal production in such environments.

[41] **Acknowledgments.** The seismic experiment was funded as part of the I-GET project by the European Union. The Geophysical Instrument Pool Potsdam provided the equipment and supporting software for field work and data recovery. We thank all participants of the field experiments for their excellent work despite the difficult climatic conditions during the survey. Special thanks go to our colleagues from the University of Pisa and the University of Milan (A. Grandi, E. Stucchi, and A. Mazzotti). Existing seismic reflection data were kindly released by Gaz de France-PEG. A. Siebert helped to review and prepare existing geological data. We appreciate the suggestions made by R. Catchings, an anonymous reviewer, and the associate editor. The I-GET consortium is thanked for excellent organization and fruitful scientific collaboration.

References

- Aichroth, B., C. Prodehl, and H. Thybo (1992), Crustal structure along the central segment of the EGT from seismic-refraction studies, *Tectonophysics*, 207, 43–64, doi:10.1016/0040-1951(92)90471-H.
- Baechler, D., T. Kohl, and L. Rybach (2003), Impact of graben-parallel faults on hydrothermal convection: The Rhine Graben case study, *Phys. Chem. Earth*, 28, 431–441, doi:10.1016/S1474-7065(03)00063-9.
- Baldschuhn, R., F. Binot, S. Fleig, and F. Kockel (2001), Tectonic Atlas of Northwest Germany and the German North Sea Sector, *Geologisches Jahrbuch, Reihe A*, 153, 3–95.
- Bauer, K., A. Schulze, T. Ryberg, S. V. Sobolev, and M. H. Weber (2003), Classification of lithology from seismic tomography: A case study from the Messum igneous complex, Namibia, *J. Geophys. Res.*, 108(B3), 2152, doi:10.1029/2001JB001073.
- Bayer, U., M. Scheck, and M. Koehler (1997), Modelling of the 3D thermal field in the northeast German basin, *Geologische Rundschau*, 86, 241–251, doi:10.1007/s005310050137.
- Benek, R., W. Kramer, T. McCann, M. Scheck, J. F. W. Negendank, D. Korich, H.-D. Huebscher, and U. Bayer (1996), Permo-Carboniferous magmatism of the Northeast German Basin, *Tectonophysics*, 266, 379–404, doi:10.1016/S0040-1951(96)00199-0.
- Bleibinhaus, F., T. Beilecke, K. Bram, and H. Gebrande (1999), A seismic velocity model for the SW Baltic Sea derived from BASIN'96 refraction seismic data, *Tectonophysics*, 314, 269–283, doi:10.1016/S0040-1951(99)00248-6.
- Eberhart-Phillips, D. (1993), Local earthquake tomography: Earthquake source regions, in *Seismic Tomography: Theory and Practice*, H. Iyer and K. Hirahara (Eds.), pp. 613–643, Chapman and Hall, New York.
- Evans, J., D. Eberhart-Phillips, and C. H. Thurber (1994), User's manual for simulp12 for imaging V_p and V_p/V_s : A derivative of the "Thurber" tomographic inversion simul3 for local earthquakes and explosions, *Open File Rep. 94-431*, U.S. Geological Survey, Washington, D. C.
- Franke, D., N. Hoffmann, and J. Kamps (1989), Alter und struktureller Bau des Grundgebirges im Nordteil der DDR, *Z. Angew. Geol.*, 35, 289–296.
- Gast, R., and T. Gundlach (2006), Permian strike slip and extensional tectonics in Lower Saxony, Germany, *Int. J. Earth Sci.*, 157, 41–55, doi:10.1127/1860-1804/2006/0157-0041.
- Hansen, M. B., M. Scheck-Wenderoth, C. Hübscher, H. Lykke-Andersen, A. Dehghani, B. Hell, and D. Gajewski (2007), Basin evolution of the northern part of the Northeast German Basin—Insights from a 3D structural model, *Tectonophysics*, 437, 1–16, doi:10.1016/j.tecto.2007.01.010.
- Hoth, K., J. Rusbült, K. Zagora, H. Beer, O. Hartmann, and S. Schretzenmayr (1993), Die tiefen Bohrungen im Zentralabschnitt der Mitteleuropäischen Senke. Dokumentation für den Zeitabschnitt 1962–1990, Schriftenreihe für Geowissenschaften, Berlin, Germany.
- Huenges, E., I. Moeck, and the Geothermal Project Group (2007), Directional Drilling and Stimulation of a Deep Sedimentary Geothermal Reservoir, *Sci. Drilling*, 5, 47–49.
- Jaritz, W. (1987), The origin and development of salt structures in north-west Germany, in *Dynamical Geology of Salt and related structures*, I. Lerche and J. J. O'Brian (Eds.), pp. 479–493, Academic Press, Orlando, FL.
- Kaiser, A., K. Reicherter, C. Hübscher, and D. Gajewski (2005), Variation of the present-day stress field within the North German Basin: insights

- from thin shell FE modeling based on residual GPS velocities, *Tectonophysics*, 397, 55–72, doi:10.1016/j.tecto.2004.10.009.
- Katzung, G. (1990), Tektonische Karte der DDR 1:500,000, Zentrales Geologisches Institut, Berlin, Germany.
- Kossow, D., C. Krawczyk, T. McCann, M. Strecker, and J. F. W. Negendank (2000), Style and evolution of salt pillows and related structures in the northern part of the Northeast German Basin, *Int. J. Earth Sci. (Geologische Rundschau)*, 89, 652–664, doi:10.1007/s005310000116.
- Lamarche, J., M. Scheck, and B. Lewerenz (2003), Heterogeneous tectonic inversion of the Mid-Polish Trough related to crustal architecture, sedimentary patterns and structural inheritance, *Tectonophysics*, 373, 75–92, doi:10.1016/S0040-1951(03)00285-3.
- Lamarche, J., and M. Scheck-Wenderoth (2005), 3D structural model of the Polish Basin, *Tectonophysics*, 397, 73–91, doi:10.1016/j.tecto.2004.10.013.
- Littke, R., U. Bayer, and D. Gajewski (2005), Dynamics of sedimentary basins: the example of the Central European Basin system, *Int. J. Earth Sci. (Geologische Rundschau)*, 94, 779–781, doi:10.1007/s00531-005-0036-8.
- Marotta, A. M., U. Bayer, and H. Thybo (2000), The legacy of the NE German Basin—reactivation by compressional buckling, *Terra Nova*, 12, 132–140, doi:10.1046/j.1365-3121.2000.123296.x.
- Maystrenko, Y., U. Bayer, and M. Scheck-Wenderoth (2005), Structure and evolution of the Glueckstadt Graben due to salt movements, *Int. J. Earth Sci. (Geologische Rundschau)*, 94, 799–814, doi:10.1007/s00531-005-0003-4.
- Michellini, A., and T. V. McEvilly (1991), Seismological studies at Parkfield, I, Simultaneous inversion for velocity structure and hypocenters using cubic b-splines parameterization, *Bull. Seismol. Soc. Am.*, 81, 524–552.
- Moeck, I., H. Schandelmeier, and H. G. Holl (2009), The stress regime in a Rotliegend reservoir of the Northeast German Basin, *Int. J. Earth Sci. (Geologische Rundschau)*, 98, 1643–1654, doi:10.1007/s00531-008-0316-1.
- Nielsen, L., H. Thybo, and M. Glendrup (2005), Seismic tomographic interpretation of Paleozoic sedimentary sequences in the southeastern North Sea, *Geophysics*, 70, R45–R56, doi:10.1190/1.1996908.
- Norden, B., and A. Förster (2006), Thermal conductivity and radiogenic heat production of sedimentary and magmatic rocks in the Northeast German Basin, *AAPG Bull.*, 90, 939–962.
- Norden, B., A. Förster, and N. Balling (2008), Heat flow and lithospheric thermal regime in the Northeast German Basin, *Tectonophysics*, 460, 215–229.
- Popp, T., and H. Kern (1998), Ultrasonic wave velocities, gas permeability and porosity in natural and granular rock salt, *Phys. Chem. Earth*, 23, 373–378, doi:10.1016/S0079-1946(98)00040-8.
- Ramm, M. (1992), Porosity-depth trends in reservoir sandstones: theoretical models related to Jurassic sandstones offshore Norway, *Mar. Petrol. Geol.*, 9, 553–567, doi:10.1016/0264-8172(92)90066-N.
- Reinhold, K., P. Krull, and F. Kockel (2008), Salzstrukturen Norddeutschlands, 1:500.000, Bundesanstalt für Geowissenschaften und Rohstoffe, Berlin/Hannover, Germany.
- Roth, F., and P. Fleckenstein (2001), Stress orientations found in north-east Germany differ from the West European trend, *Terra Nova*, 13, 289–296, doi:10.1046/j.1365-3121.2001.00357.x.
- Scheck, M., L. Barrio-Alvers, U. Bayer, and H.-J. Götze (1999), Density structure of the Northeast German Basin: 3D modeling along the DEKORP Line BASIN96, *Phys. Chem. Earth*, 24, 221–230, doi:10.1016/S1464-1895(99)00022-8.
- Scheck, M., and U. Bayer (1999), Evolution of the Northeast German Basin: Inferences from a 3D structural model and subsidence analysis, *Tectonophysics*, 313, 145–169, doi:10.1016/S0040-1951(99)00194-8.
- Scheck, M., U. Bayer, and B. Lewerenz (2003a), Salt movements in the Northeast German basin and its relation to major post-Permian tectonic phases: Results from 3D structural modeling, backstripping and reflection seismic data, *Tectonophysics*, 361, 277–299, doi:10.1016/S0040-1951(02)00650-9.
- Scheck, M., U. Bayer, and B. Lewerenz (2003b), Salt redistribution during extension and inversion inferred from 3D backstripping, *Tectonophysics*, 373, 55–73, doi:10.1016/S0040-1951(03)00283-X.
- Scheck, M., U. Bayer, V. Otto, J. Lamarche, D. Banka, and T. Pharaoh (2002), The Elbe Fault System in North Central Europe: A basement controlled zone of crustal weakness, *Tectonophysics*, 360, 281–299, doi:10.1016/S0040-1951(02)00357-8.
- Scheck-Wenderoth, M., and J. Lamarche (2005), Crustal memory and basin evolution in the Central European basin System: New insights from a 3D structural model, *Tectonophysics*, 397, 143–165, doi:10.1016/j.tecto.2004.10.007.
- Schoen, J. H. (1996), Physical properties of rocks: Fundamentals and principles of petrophysics, *Handbook of Geophys. Explor., Seismic Explor.*, vol. 18, Pergamon, New York.
- Schulze, A., and E. Lück (1992), Some results of deep seismic investigations in East Germany, *Phys. Earth Planet. Inter.*, 69, 231–238, doi:10.1016/0031-9201(92)90140-Q.
- Somerton, W. (1992), Thermal Properties and Temperature-Related Behavior of Rock/Fluid Systems, Elsevier, New York.
- Thurber, C. H. (1983), Earthquake locations and three-dimensional crustal structure in the Coyote Lake area, central California, *J. Geophys. Res.*, 88, 8226–8236.
- Thurber, C. H. (1993), Local earthquake tomography: Velocities and v_p/v_s -theory, in *Seismic Tomography: Theory and Practice*, H. Iyer and K. Hirahara (Eds.), pp. 563–583, Chapman and Hall, New York.
- Toomey, D. R., and G. R. Foulger (1989), Tomographic inversion of local earthquake data from the Hengill-Grensdalur central volcano complex, Iceland, *J. Geophys. Res.*, 94, 17,497–17,510, doi:10.1029/JB094iB12p17497.
- Van Wees, J. D., R. A. Stephenson, P. A. Ziegler, U. Bayer, T. McCann, R. Dadlez, R. Gaupp, M. Narkiewicz, F. Bitzer, and M. Scheck (2000), On the origin of the South Permian Basin, Central Europe, *Mar. Petrol. Geol.*, 17, 43–59, doi:10.1016/S0264-8172(99)00052-5.
- Zelt, C. A. (1998), Lateral velocity resolution from three-dimensional seismic refraction data, *Geophys. J. Int.*, 135, 1101–1112, doi:10.1046/j.1365-246X.1998.00695.x.
- Zelt, C. A., A. Azaria, and A. Levander (2006), 3D seismic refraction travel time tomography at a groundwater contamination site, *Geophysics*, 71, H67–H78, doi:10.1190/1.2258094.
- Zelt, C. A., and R. B. Smith (1992), Seismic travel time inversion for 2-D crustal velocity structure, *Geophys. J. Int.*, 108, 16–34, doi:10.1111/j.1365-246X.1992.tb00836.x.
- Ziegler, P. A. (1990), Geological Atlas of Western and Central Europe, 2nd ed. Shell Int. Petroleum Mij BV and Geol. Soc. of London (London), 1–239.
- Ziegler, P. A., and P. Dezès (2006), Crustal evolution of western and central Europe, in *European Lithosphere Dynamics*, D. G. Gee and R. A. Stephenson (Eds.), pp. 43–56, Geological Society, London, U. K.

K. Bauer, I. Moeck, B. Norden, A. Schulze, and M. Weber, Deutsches GeoForschungsZentrum GFZ, Telegrafenberg, 14473 Potsdam, Germany. (Klaus@gfz-potsdam.de)

H. Wirth, Bundesanstalt für Geowissenschaften und Rohstoffe (BGR), Wilhelmstr. 25–30, 13593 Berlin, Germany.